A single grain boundary parameter to characterize normal stress fluctuations in materials with elastic cubic grains

Samir El Shawish, Timon Mede, Jeremy Hure

Available online at www.sciencedirect.com
ScienceDirect
ELSEVIER
00 (2020) 1–29

A single grain boundary parameter to characterize normal stress fluctuations in materials with elastic cubic grains

S. El Shawish[a,*], T. Mede[a], J. Hure[b]

[a] *Jožef Stefan Institute, SI-1000, Ljubljana, Slovenia*
[b] *Université Paris-Saclay, CEA, Service d'Études des Matériaux Irradiés, 91191 Gif-sur-Yvette cedex, France*

Abstract

A finite element analysis of intergranular normal stresses is performed in order to identify a possible *statistical* correlation between the intergranular normal stresses and the corresponding grain boundary type within a polycrystalline aggregate. Elastic continuum grains of cubic lattice symmetry are assumed in the analysis. Meaningful results are obtained by analyzing the first two statistical moments of grain boundary normal stresses obtained on several grain boundary types.

Among the five macroscopic parameters (5D) describing a grain boundary, the orientation of the grain boundary plane relative to the two adjacent crystal lattices (4D) is found to be the most important property influencing the normal stresses. To account for it, a single new (1D) parameter E_{12} is introduced, which combines the geometrical aspect of grain boundary with its material properties and measures the average stiffness of grain boundary neighborhood along the grain boundary normal direction. It is demonstrated that E_{12}, in combination with Zener elastic anisotropy index A, is able to accurately predict normal stress fluctuations on any grain boundary type in a material with cubic lattice symmetry. It is argued that largest normal stresses most likely form on grain boundaries whose normals are oriented along the stiffest direction in both adjacent grains (<111> for crystals with $A > 1$ or <001> for crystals with $A < 1$). Moreover, it is shown that classification of grain boundaries according to their propensity to exhibit large normal stresses can be trivially reduced to the (analytical) calculation of the corresponding effective stiffness parameter E_{12}.

A few practical implications are discussed relevant to intergranular stress-corrosion cracking of Coincidence Site Lattice grain boundaries. For example, it is highlighted that in face-centered cubic materials the coherent Σ3 twin grain boundaries, which are known for their very high cracking resistance, nevertheless exhibit largest intergranular normal stresses, indicating that cracking resistance is associated with high grain boundary strength.

Keywords: IGSCC, grain boundary type, coincidence site lattice, intergranular normal stress fluctuations, finite element method, grain boundary engineering

1. Introduction

Due to their strength, stiffness, fracture toughness and resistance to high temperatures metallic alloys remain the structural material of choice in various industries. But their susceptibility to ageing effects and material degradation can shorten the total service life of components made from them. One of the most significant material degradation modes responsible for initiation and propagation of cracks along the grain boundaries (GBs) is the intergranular stress corrosion cracking (IGSCC). IGSCC has been observed experimentally for a wide range of materials, for example, in austenitic stainless steels (Nishioka et al., 2008; Le Millier et al., 2013; Stephenson and Was, 2014; Gupta et al., 2016; Fujii et al., 2019), zirconium alloys (Cox, 1970, 1990), nickel based alloys (Van Rooyen, 1975; Shen and Shewmon,

*Corresponding author
Email addresses: samir.elshawish@ijs.si (S. El Shawish), timon.mede@ijs.si (T. Mede), jeremy.hure@cea.fr (J. Hure)

1990; Panter et al., 2006; IAEA, 2011), high strength aluminum alloys (Speidel, 1975; Burleigh, 1991) and ferritic steels (Wang and Atrens, 1996; Arafin and Szpunar, 2009).

In recent years, many studies have been conducted to analyze the susceptibility of various materials to IGSCC initiation from experimental, analytical and numerical viewpoints. It is now well accepted that IGSCC occurs under the conjoint action of material properties, aggressive environment, and mechanical forces. From the material aspect, the susceptibility to IGSCC has been investigated on different GB types and GB networks using the electron backscatter diffraction (EBSD) measurements. Restricting to austenitic stainless steel, efforts have been made to clarify the initiation of intergranular cracks on Σn GBs based on the Coincidence Site Lattice (CSL) model. It was concluded (Gertsman and Bruemmer, 2001) that crack initiation could not be explained using only Σn GB types as cracks occurred even at some Σn GBs with small n, including Σ3 GBs, in stainless steel alloys. Studies on type 304 stainless steel (Rahimi and Marrow, 2011; Fujii et al., 2019) established that GB type and grain size significantly influence the susceptibility to IGSCC. The influence of GB arrangement on IGSCC susceptibility was investigated in stainless steels of type 304 (Rahimi et al., 2009) and type 316 (Liu et al., 2019) where it was shown that IGSCC resistance could be improved by increasing the fraction of twin or twin-related (Σ3) GBs.

On the mechanical side, intergranular normal stresses (INS) have been found to play a significant role in IGSCC initiation. Few approaches have been applied to characterize the initiation of IGSCC. A simple Schmid-Modified Grain Boundary Stress (SMGBS) model was proposed (West and Was, 2011) to investigate the initiation of an intergranular crack based on a normal stress acting at GB. The SMGBS model considers the combined effects of GB plane orientation and grain orientations through their Schmid factors. It was pointed out that intergranular cracks occur most likely at highly stressed GBs. In other similar studies (Stratulat et al., 2014; Zhang et al., 2019; Fujii et al., 2019) the SMGBS model was used to discuss crack initiation in austenitic stainless steel. It was concluded that initiation sites coincide with the most highly stressed GBs. Also, by measuring local stresses in irradiated iron based alloys using high-resolution EBSD technique (Johnson et al., 2019), a criterion for crack initiation was proposed using normal stresses acting at GBs.

The experimental and analytical studies have been supplemented by various numerical simulations. Focusing on the mechanical aspect, crystal plasticity finite element model (CPFEM) simulations (Diard et al., 2002, 2005; Kanjarla et al., 2010; Gonzalez et al., 2014; Hure et al., 2016; El Shawish and Hure, 2018) and crystal plasticity fast Fourier transform (CPFFT) simulations (Lebensohn et al., 2012; Liang et al., 2020) were used to obtain intergranular stresses in either synthetic or realistic polycrystalline aggregates, providing valuable information for IGSCC initiation. INS were found to depend on elasto-plastic anisotropy of grains with either cubic (Gonzalez et al., 2014; Hure et al., 2016; El Shawish and Hure, 2018) or hexagonal lattice symmetries (El Shawish and Hure, 2018). Based on results of a recent systematic CPFEM study (El Shawish and Hure, 2018), a new phenomenological relationship was discovered for standard deviation of INS evaluated on random GBs within a polycrystalline aggregate under external loading. With such a relation, the probability of finding GB stress exceeding a critical value (related to GB strength) could be assessed, thus providing a quick and reliable tool for estimating the propensity of an aggregate to develop high INS without having to perform CPFEM simulations.

As different GB types (defined by five macroscopic degrees of freedom) show different IGSCC sensitivities in a given material, it would be useful to know how much of this behavior results solely from the difference in their associated GB strengths or there exists also some sizable variation of INS across the GB types. In this respect, a possible correlation between a particular GB type and the corresponding INS distribution evaluated on it is investigated in this study. Knowing how GB normal stresses (in addition to GB strengths) vary with a particular GB type in a given polycrystal would provide a better understanding of both the material and loading aspects of IGSCC susceptibility. Such study appears to be the key ingredient towards IGSCC initiation modelling and is therefore the main objective of this paper.

To identify a possible statistical correlation between the INS and the corresponding GB type embedded within a polycrystalline aggregate, finite element analysis of INS is performed in 3D periodic Voronoi aggregates composed of elastic grains of cubic lattice symmetry and under uniaxial macroscopic loading. To obtain meaningful results, first two statistical moments, the mean value and standard deviation, are analyzed from the calculated INS distributions obtained on GBs of a certain type. Since material and mechanical aspects of IGSCC are jointly addressed (but decoupled from the environmental factors hidden in the GB strength related to critical GB stresses), this study may be also relevant for other degradation mechanisms where INS is the driving force for crack initiation leading to intergranular fracture (*e.g.*, mechanical and thermal fatigue). To allow for such generalization, a large set of different

cubic materials is investigated and compared.

The reason for using elastic grains in the analysis is twofold. First, there are several applications that involve purely elastic strains induced by small applied stresses or stresses close to yield stress. For example, fatigue damage initiation considers purely elastic loads, while IGSCC initiation is usually related to stresses at or slightly below yield stress (Gupta et al., 2016). Secondly, the INS distributions evaluated at the onset of plasticity deviate very gradually from those calculated under purely elastic loads (El Shawish and Hure, 2018). This implies that elastic INS distributions studied here may be relevant for an even broader set of mechanical applications. Nevertheless, having purely elastic grains also requires much fewer assumptions about constitutive modelling, which may sometimes be hard to justify unless some additional experimental validation is provided.

2. Models and method

2.1. Constitutive model

The anisotropic elasticity of crystals with cubic symmetry is governed by the generalized Hooke's law, $\sigma_{ij} = C_{ijkl}\epsilon_{kl}$, where the stiffness tensor C_{ijkl} is composed of three independent elastic constants (in Voigt notation), C_{11}, C_{12}, C_{44}, whose values are shown for several cubic crystals in Tab. 1.

Crystal	C_{11}	C_{12}	C_{44}	A	A^u
Mo	440.8	172.4	121.7	0.91	0.01
Al	107.3	60.9	28.3	1.22	0.05
Cr	339.8	58.6	99.0	0.70	0.15
Pt	346.7	250.7	76.5	1.59	0.27
Nb	240.2	125.6	28.2	0.49	0.63
α-Fe	231.4	134.7	116.4	2.41	0.99
Ni	246.5	147.3	127.4	2.57	1.15
Au	192.9	163.8	41.5	2.85	1.44
Cu	168.4	121.4	75.4	3.21	1.82
γ-Fe	197.5	125.0	122.0	3.37	2.00
Pb	49.5	42.3	14.9	4.14	2.86
Nb*	240.2	125.6	11.46	0.20	3.84
Li	13.5	11.44	8.78	8.52	7.97
Na	6.15	4.96	5.92	9.95	9.66
Nb**	240.2	125.6	5.73	0.10	9.72

Table 1. Elastic constants C_{ij} in Voigt notation (in units of GPa), Zener elastic anisotropy index A (Zener, 1948) and universal elastic anisotropy index A^u (Ranganathan and Ostaja-Starzewski, 2008) for cubic crystals used in this study. Elastic constants are taken from (Bower, 2010). Nb* and Nb** are fictitious materials representing Nb with modified C_{44} to obtain $A = 0.20$ and $A = 0.10$, respectively. Materials are ordered according to A^u.

Materials in Tab. 1 are ordered according to their universal elastic anisotropy index A^u (Ranganathan and Ostaja-Starzewski, 2008) where $A^u = 0$ denotes isotropic crystal. For comparison, also Zener elastic anisotropy index A (Zener, 1948) is added

$$A = \frac{2C_{44}}{C_{11} - C_{12}} \tag{1}$$

with $A = 1$ denoting isotropic crystal.

To study elastic INS distributions on different special GBs, elastic grains with γ-Fe properties are assumed in Sec. 3 and used as a reference material throughout the paper. In Sec. 4, however, also other cubic materials from Tab. 1 are investigated.

The constitutive equations of the generalized Hooke's law were solved with finite element solver Abaqus (Simulia, 2016) using small strain approximation.

2.2. Aggregate model generation

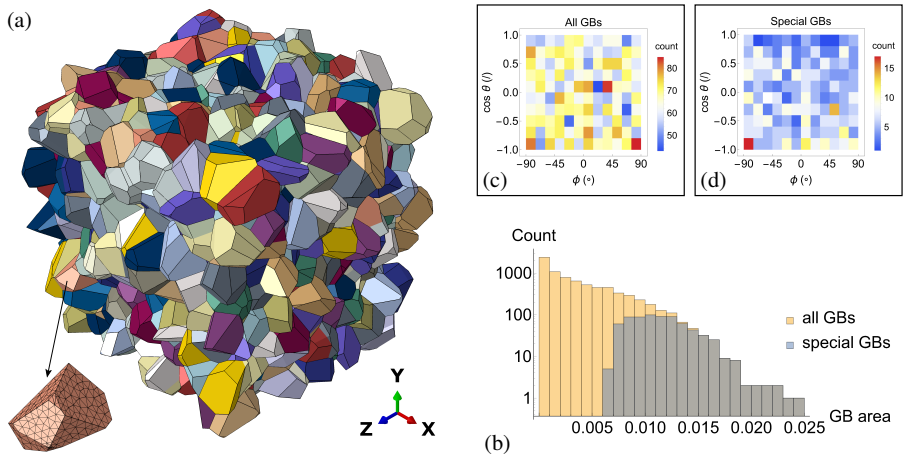

Figure 1. (a) Periodic Voronoi aggregate model with 1000 grains used in this study. Different grains are denoted by different colors. Finite element mesh is shown on one selected grain. Total number of elements in the model is 1263042. (b) Histogram showing distribution of GB areas in arbitrary units (note the logarithmic scale). Special GBs are selected among GBs with largest area. Total number of GBs is 7762 and the number of special GBs is either 709 (representing 28% GB area) or 419 (17% GB area). 2D distributions of GB normals, $\boldsymbol{n} = (\sin\theta\cos\phi, \sin\theta\sin\phi, \cos\theta)$, accounting for either all GBs (c) or only special GBs (d) are both approximately uniform.

Polycrystal aggregate models were generated upon Voronoi tessellations using software package Neper (Quey et al., 2011) to build the periodic microstructures in all three spatial directions. The arrangement of grains was based on a Poisson-Voronoi diagram. Finite element meshes were also generated with Neper using quadratic tetrahedral elements (C3D10) to preserve the geometry of the grains.[1] An example of the model with 1000 grains used throughout this study is shown in Fig. 1(a).

The periodic boundary conditions were implemented along all three aggregate principal directions (El Shawish et al., 2020) and a uniaxial loading was applied along direction 1 (x axis), providing a single nonzero macroscopic stress component, $\Sigma_{11} = \langle\sigma_{11}\rangle > 0$. Here, the averaging $\langle.\rangle$ was performed over the entire volume of the model. As grains were assumed to be purely elastic, a unit loading was applied using a small strain approximation.

2.3. Grain boundary type assignment

Same elastic material properties of γ-Fe were assigned to all the grains of the model but each time with different crystallographic orientations to model aggregates with various GB types.

On a macroscopic (continuum) level, a GB can be characterized by five degrees of freedom (DOF), following two standard approaches. In the first approach, three parameters are used to specify a rotation between the crystal lattices of the two neighboring grains (*e.g.*, using either three Euler angles or misorientation angle and axis) and two parameters to specify GB boundary plane. Alternatively, one can use four parameters to define a GB plane in the coordinate system of each of the two grains and one additional parameter to describe a twist angle (with respect to GB normal) between the neighboring crystal lattices.

It is important to note that external loading implies additional DOF per GB. For example, in the case of applied tensile stress two additional DOF should be considered to uniquely characterize a GB. In this study, however, the effect of a GB tilt relative to the applied tensile direction is studied statistically by evaluating GB stresses on a large number of randomly oriented GBs (see also further discussion). In this way, the two additional DOF per GB are integrated out and only five DOF per GB are retained in the model. Note that at smaller (atomistic) scales even more DOF per GB would be required, for example, to describe the arrangement of atoms on both sides of the GB plane (*e.g.*, coherent vs. non-coherent GBs).

[1] We note that quadratic tetrahedral elements (C3D10) were not supported by Neper (Quey et al., 2011) when used in combination with periodic geometries, therefore an in-house script was developed to generate second-order meshes with proper node connectivity at the free surfaces.

Following the above discussion, a random aggregate is defined here as a Voronoi aggregate with purely *random* GBs. In practice, this is achieved by assigning random grain orientations to all the grains to provide a random crystallographic texture. In this case, the resulting 1D distribution of misorientation angles approaches a well-known curve for a randomly textured polycrystal with cubic lattice symmetry (Mackenzie, 1958).

Unlike random GBs, *special* GBs are defined as GBs with the value of at least one chosen DOF set. The simplest example would be a misorientation GB type where a misorientation angle (one DOF) between the two grains is fixed to a certain value while the remaining four DOF are left random. It is expected that the effect of special GBs is larger when more DOF are fixed (thus having fewer random DOF).

To generate a non-random aggregate, a relatively small fraction η of GBs is assigned a special GB character while the remaining fraction $1-\eta$ is retained as random GBs[2]. The fraction η in fact denotes a ratio between the area of all special GBs and the area of all GBs employed in the model. To improve statistical evaluations presented later on, special GBs were selected from the largest available GBs of the aggregate. This is depicted in histogram on Fig. 1(b) where a special GB area distribution is shown to overlap with the right-hand side of a all-GB area histogram distribution. In this way, $\eta_{max} \approx 0.28$ and $\eta_{max} \approx 0.17$ were reached in practice (with the limiting factor being the topology of the grains in 3D) for respectively fixing up to three DOF and more than three DOF per special GB. By comparing 2D distributions of GB normals in Figs. 1(c,d), special GBs as well as all GBs are shown to be more or less randomly oriented in space with no preferred inclination.

Table 2 lists and describes all the different types of special GBs investigated in this study. The visualization of some of the most common special GBs is given for one particular grain pair in Appendix A.

Special GB	Definition	fixed DOF	GB plane	Fraction	Comment
misorientation	fixed misorientation around random axis	1	no	0.28	Fig. A.14(a,b)
twist	fixed rotation around $\boldsymbol{n}$	3	yes	0.28	
Σ3	60.0000° rotation around <111>	3	no	0.28	
Σ5	36.8699° rotation around <100>	3	no	0.28	
Σ7	38.2132° rotation around <111>	3	no	0.28	
Σ9	38.9424° rotation around <110>	3	no	0.28	
Σ11	50.4788° rotation around <110>	3	no	0.28	
Σ3-twist	60.0000° rotation around <111> $\parallel \boldsymbol{n}$	5	yes	0.17	Fig. A.14(d)
Σ5-twist	36.8699° rotation around <100> $\parallel \boldsymbol{n}$	5	yes	0.17	Fig. A.14(f)
Σ7-twist	38.2132° rotation around <111> $\parallel \boldsymbol{n}$	5	yes	0.17	Fig. A.14(h)
Σ9-twist	38.9424° rotation around <110> $\parallel \boldsymbol{n}$	5	yes	0.17	Fig. A.14(j)
Σ11-twist	50.4788° rotation around <110> $\parallel \boldsymbol{n}$	5	yes	0.17	Fig. A.14(l)
Σ3-twin	60.0000° sym. rotation around <111> $\perp \boldsymbol{n}$	5	yes	0.17	Fig. A.14(c)
Σ5-twin	36.8699° sym. rotation around <100> $\perp \boldsymbol{n}$	5	yes	0.17	Fig. A.14(e)
Σ7-twin	38.2132° sym. rotation around <111> $\perp \boldsymbol{n}$	5	yes	0.17	Fig. A.14(g)
Σ9-twin	38.9424° sym. rotation around <110> $\perp \boldsymbol{n}$	5	yes	0.17	Fig. A.14(i)
Σ11-twin	50.4788° sym. rotation around <110> $\perp \boldsymbol{n}$	5	yes	0.17	Fig. A.14(k)
<*abc*>-twist	fixed rotation around <*abc*> $\parallel \boldsymbol{n}$ considered axes: <001>, <101>, <111>	5	yes	0.17	Fig. A.14(n,p,r)
<*abc*>-twin	fixed sym. rotation around <*abc*> $\perp \boldsymbol{n}$ considered axes: <001>, <101>, <111>	5	yes	0.17	Fig. A.14(m,o,q)
(*abc*)-(*def*)	grain 1: [*abc*] $\parallel \boldsymbol{n}$, grain 2: [*def*] $\parallel \boldsymbol{n}$ considered planes: (001), (104), (114), (102), (214), (112), (304), (314), (324), (334), (101), (414), (212), (434), (111)	4	yes	0.17	Fig. A.14(s-x)

Table 2. List of investigated special GBs and their definitions. GB plane column denotes if GB plane is involved in the definition of a special GB. $\boldsymbol{n}$ stands for a GB normal. Fraction value η denotes a ratio between the area of all GBs of a special type investigated and the area of all GBs employed in the model. Twin GBs in Σn-twin and <*abc*>-twin are defined as symmetric tilt GBs.

[2]Here, a GB is understood as a Voronoi facet.

The assignment of special GB orientations was performed with in-house Mathematica script (Wolfram Research). A practical distinction was made between special GBs with a fixed GB plane (*e.g.*, Σn-twist, Σn-twin or (*abc*)-(*def*)) and those that do not specify its orientation (*e.g.*, misorientation or Σn). In the former case, additional geometrical inputs in the form of GB planes were needed and provided by the model generation software Neper.

It is important to note that same grain topology and finite element mesh (see Fig. 1(a)) were employed in all considered aggregate models from Tab. 2. In this way the effects of using different special GB types were isolated from other possible finite size effects studied separately in Appendix B.

2.4. Intergranular normal stress calculation

Intergranular normal stress (INS) distributions were calculated over all special GBs of one particular type in order to evaluate their response in comparison to random GBs. The used methodology for the calculation of INS has been successfully implemented before (Hure et al., 2016; El Shawish and Hure, 2018; El Shawish et al., 2020).

For each pair i of quadratic (C3D10) tetrahedral elements touching a GB plane k with their two facets, a GB facet area A_i^k and GB normal $\boldsymbol{n}_k$ were identified first. In both elements, six Cauchy stress tensors, $\boldsymbol{\sigma}_{i,1} \dots \boldsymbol{\sigma}_{i,6}$, were then obtained at the corresponding Gauss points located closest to the GB plane. These were then used to calculate one single normal stress value per element pair, $\sigma_{i,nn}^k = 1/6 \sum_{j=1}^{6} \boldsymbol{n}_k.\boldsymbol{\sigma}_{i,j}.\boldsymbol{n}_k$. As elements of different size were used in the finite element mesh, the occurrence of $\sigma_{i,nn}^k$ in the computation of the INS distribution was weighted by the surface A_i^k of the GB facet on which it was obtained. Finally, the first two statistical moments, the mean and the standard deviation, were calculated to characterize the distribution using the following two relations $\langle \sigma_{nn} \rangle = \sum_k \sum_i A_i^k \sigma_{i,nn}^k / \sum_k \sum_i A_i^k$ and $s(\sigma_{nn}) = \sqrt{\langle \sigma_{nn}^2 \rangle - \langle \sigma_{nn} \rangle^2}$, respectively. Here, the summation k was performed over all special GBs of a non-random aggregate (unless stated differently) or over all GBs of a random aggregate. The two statistical quantities were further normalized by macroscopic tensile stress $\Sigma = \Sigma_{11}$ to obtain $\langle \sigma_{nn}/\Sigma \rangle$ and $s(\sigma_{nn}/\Sigma)$ shown hereafter.

In Appendix B the above method is shown to be robust and accurate enough to provide converged $s(\sigma_{nn}/\Sigma)$ upon refining the finite element mesh.

Before addressing the results of the study, it may be useful to mention all relevant sources that may contribute to the width of INS distribution when evaluated on one particular GB type:

- The main source is expected to be coming from the random orientation of special GB planes. In an ideal case of a sufficiently large aggregate, special GB normals $\boldsymbol{n}$ would be distributed uniformly on a sphere. In the absence of material anisotropy, INS can be expressed as $\sigma_{nn}/\Sigma = \cos^2 \theta$ where θ denotes the angle between GB normal and applied uniaxial loading direction. The corresponding probability density function is $1/(2\sqrt{\sigma_{nn}/\Sigma})$ where σ_{nn} is trivially bounded by Σ, and first two statistical moments are $\langle \sigma_{nn}/\Sigma \rangle = 1/3$ and $s(\sigma_{nn}/\Sigma) = 2/(3\sqrt{5}) \approx 0.298$. Irrespective of the material anisotropy, largest INS is expected to appear on GBs with GB normal closely aligned with the applied uniaxial loading direction ($\theta \sim 0$).[3]

- Another important source of distribution width is the already mentioned material elastic anisotropy. When the mismatch effects between adjacent grains become important, the INS distribution adopts a bimodal shape with largest INS exceeding the upper bound Σ. As explained in (El Shawish and Hure, 2018), the distribution broadening, measured by $s(\sigma_{nn}/\Sigma)$, becomes well correlated with the elastic anisotropy of the grains, implying that universal elastic anisotropy index (Ranganathan and Ostaja-Starzewski, 2008) can be used to assess the potential susceptibility of random aggregates to IGSCC. The effect of material anisotropy on $s(\sigma_{nn}/\Sigma)$ in non-random aggregates is discussed in more detail in Sec. 4.

- The last important source is related to the special GB type, which has, by definition, at least one fixed DOF. Since the remaining DOF are left random, it is expected that special GBs with fewer random DOF would provide larger effect on INS distribution. In fact, it is the goal of this study to identify a possible statistical correlation between the specific GB type and the corresponding INS distribution. Such information would be valuable to various fields of research and engineering, including material characterization and GB engineering.

[3] Local stress concentrations are expected also on other GBs in close proximity to geometric discontinuities such as grain edges or triple points.

3. Analysis of γ-Fe grains

This section presents INS distributions and corresponding statistical moments calculated on various special GBs using finite element simulations of random and non-random polycrystalline aggregates composed of γ-Fe grains under tensile loading.

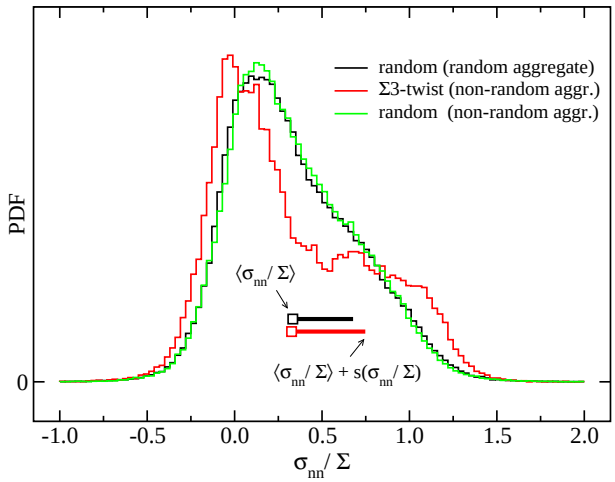

Figure 2. Probability density functions (PDF) of normalized INS σ_{nn}/Σ calculated in two geometrically equivalent Voronoi aggregate models composed of γ-Fe grains under tensile stress Σ. A comparison is shown between an aggregate with purely random GBs and an aggregate with 17% GB area corresponding to Σ3-twist GBs (and the remaining 83% GB area to random GBs). In the former case, the distribution is calculated on all GBs, whereas in the latter case two distributions are calculated on either Σ3-twist GBs or random GBs (due to poorer statistics PDF of Σ3-twist GBs is less smooth). To characterize the distributions, the corresponding mean values and standard deviations are depicted on a graph by square symbols and horizontal error bars.

Figure 2 thus juxtaposes the distribution of INS on random GBs with that obtained on Σ3-twist GBs. Here, Σ3-twist GB was chosen to be a representative special GB because it is a well-known GB found in face-centered cubic metals that has a very low GB energy (An et al., 2018; Fujii et al., 2019). It is often called a coherent Σ3 twin GB as all atoms at the boundary belong to both crystals.[4] Because all lattice sites on the GB are coincidence sites and there is no lattice strain or excess volume associated with the GB, coherent Σ3 twin GBs show very high corrosion resistance (An et al., 2018).

It is rather surprising to observe on Fig. 2 that probability density function of σ_{nn}/Σ is considerably wider for Σ3-twist GBs than for random GBs. Wider distribution also implies there is a higher fraction of Σ3-twist GBs with larger INS (for the same applied stress Σ), which may seem counterintuitive as these GBs are known for their high cracking resistance. However, it needs to be noted that GB crack initiation depends not only on local GB stress σ_{nn} but also (or mostly) on local GB strength. In a simple picture, crack initiation starts when $\sigma_{nn} > \sigma_c$, where critical local stress σ_c is associated with GB strength. As only the loading part is addressed here, the knowledge of GB strength of Σ3-twist GBs should resolve this seeming inconsistency. Namely, very low energy of GBs is generally associated with their enhanced strength, therefore an increase of σ_{nn} due to specific GB type does not necessarily increase its propensity for cracking.

[4] As already pointed out, a coherency of GBs relates to atomistic DOF which are excluded from the current continuum framework.

3.1. Density of special grain boundaries

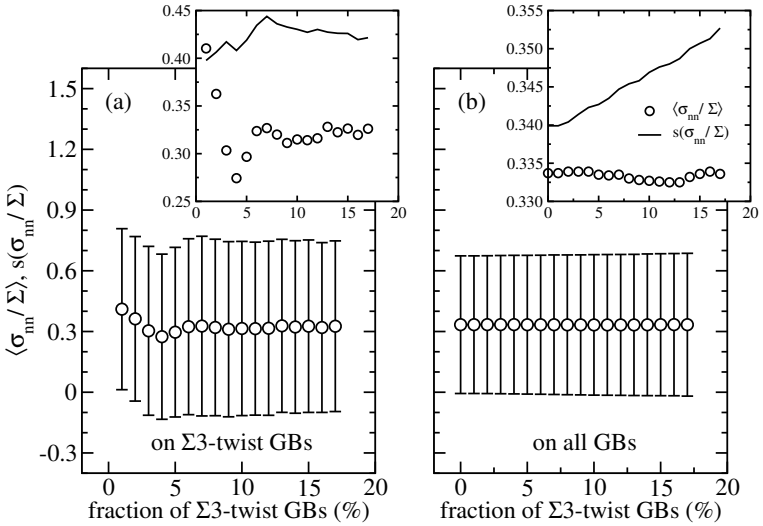

Figure 3. Mean value $\langle\sigma_{nn}/\Sigma\rangle$ and standard deviation $s(\sigma_{nn}/\Sigma)$ of normalized INS, plotted as a function of GB area fraction of Σ3-twist GBs (with the remaining area fraction corresponding to random GBs). Results in (a) are calculated on Σ3-twist GBs only and in (b) on all GBs. Insets show the same information but on a different scale. Material properties of γ-Fe were used.

The effect of area fraction η of Σ3-twist GBs is studied in Fig. 3, where first two statistical moments $\langle\sigma_{nn}/\Sigma\rangle$ and $s(\sigma_{nn}/\Sigma)$ are plotted as a function of η (with $\eta_{max} = 0.17$ and the remaining $1 - \eta$ GB area corresponding to random GBs) in a Voronoi aggregate under elastic tensile stress Σ. A comparison is shown between the two cases where the two moments are calculated either only on Σ3-twist GBs (Fig. 3(a)) or on all GBs (Fig. 3(b)). In the former case, both $\langle\sigma_{nn}/\Sigma\rangle$ and $s(\sigma_{nn}/\Sigma)$ show oscillations at smaller fractions $\eta \lesssim 0.08$. These oscillations are attributed to insufficient number of special GBs present in the model, which constitute a non-uniform distribution of GB normals. Note that $\eta = 0.05$ and $\eta = 0.10$ correspond to respectively 88 and 202 special GBs in an aggregate with a total of 7762 GBs. Observed fluctuations are therefore finite size effects that should diminish with growing aggregate size.

The fact that both statistical moments, calculated solely on special GBs, seem to converge (or at least do not change significantly) with increasing fraction of special GBs ($\eta \gtrsim 0.08$), suggests that elastic interactions between GBs are relatively short ranged. In particular, even at a given maximal fraction of $\eta = 0.17$, special GBs seem to be placed sufficiently far apart (with enough random GBs placed in between) to have a negligible impact on each other.

Short range interactions between (special) GBs are further confirmed in Fig. 3(b), where the effect of adding more Σ3-twist GBs into the model results in a slight linear increase of $s(\sigma_{nn}/\Sigma)$ when calculated on all GBs. However, the overall effect is expectedly small because the main contribution still comes from random GBs.

From Fig. 3 it also appears that $\langle\sigma_{nn}/\Sigma\rangle \approx 1/3$ for any sufficiently high η. As will be evident later on, this observation actually holds for all considered special GBs. As a practical implication, one may thus focus predominantly on INS fluctuations measured by $s(\sigma_{nn}/\Sigma)$.

Since the fraction of special GBs η has no significant effect (except at very low $\eta \lesssim 0.08$ due to finite size effects) on the first two statistical moments calculated on special GBs, all the following results are shown for η_{max} (either 0.17 or 0.28) in order to get statistically more relevant results. In the following, the effect of different special GBs is analyzed and compared.

3.2. Coincidence site lattice grain boundaries

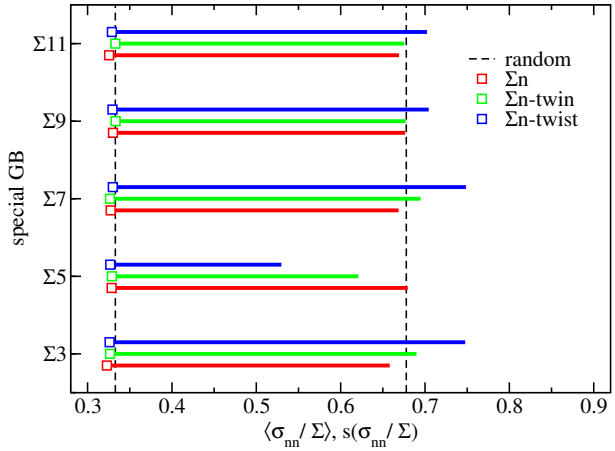

Figure 4. Mean value and standard deviation of normalized INS, $\langle\sigma_{nn}/\Sigma\rangle$ and $s(\sigma_{nn}/\Sigma)$, plotted for five simplest Coincidence Site Lattice GBs Σn ($n = 3, 5, 7, 9, 11$) representing 28% (for Σn) and 17% (for Σn-twin/twist) GB area fractions. Dashed lines denote values obtained in the same aggregate model but with purely random GBs. Material properties of γ-Fe were used.

Figure 4 shows the effect of five lowest Coincidence Site Lattice (CSL) GBs ($n = 3, 5, 7, 9, 11$) embedded in the Voronoi aggregate model under tensile stress Σ. Besides the usual Σn GB that is defined by specific misorientation axis and misorientation angle, also Σn-twin and Σn-twist GBs with the additional constraints on GB plane (see Tab. 2) are included in the comparison. Since Σn GB has three fixed DOF (that have no connection to the GB normal) and two random DOF, the corresponding standard deviation $s(\sigma_{nn}/\Sigma)$ is similar to that of a random GB. On the contrary, both Σn-twin and Σn-twist GBs have all five DOF fixed, which makes their responses substantially different from that of a random aggregate. Nevertheless, the largest effects among the two GB types are observed for Σn-twist GBs, where Σ3-twist and Σ7-twist GBs produce considerably larger INS fluctuations with $s(\sigma_{nn}/\Sigma) \approx 0.42$ and Σ5-twist GBs considerably smaller INS fluctuations with $s(\sigma_{nn}/\Sigma) \approx 0.20$. As will be shown later, these two values represent (approximately) the maximal and the minimal $s(\sigma_{nn}/\Sigma)$ of a polycrystal composed of γ-Fe grains.

3.3. Grain boundaries with fixed plane

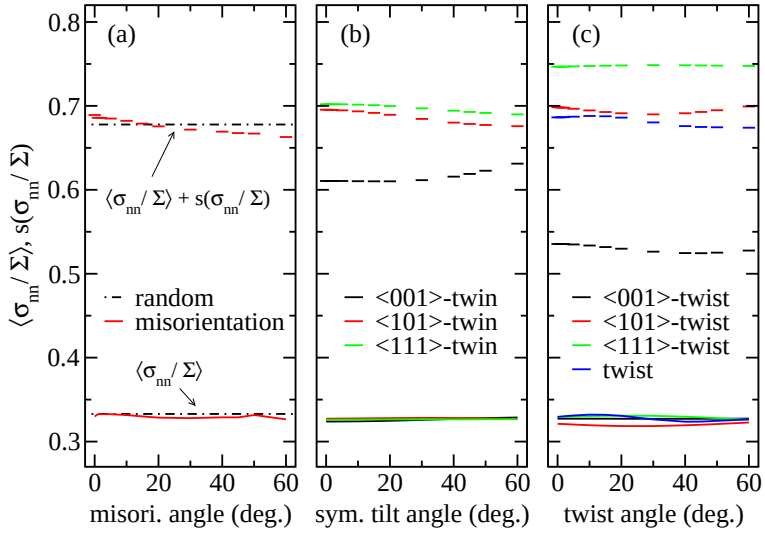

Figure 5. Mean value and standard deviation of normalized INS, $\langle\sigma_{nn}/\Sigma\rangle$ and $s(\sigma_{nn}/\Sigma)$, plotted as a function of (a) misorientation angle specifying misorientation GBs, (b) symmetric tilt angle specifying <*abc*>-twin GBs, and (c) twist angle specifying <*abc*>-twist and twist GBs. Same Voronoi aggregate model composed of γ-Fe grains and under tensile stress Σ is used in all calculations. Dashed lines in (a) denote values obtained in the same aggregate but with purely random GBs.

In Fig. 5 the first two statistical moments are shown for various special GBs that depend on a misorientation angle (Fig. 5(a)), symmetric tilt angle (Fig. 5(b)) or twist angle (Fig. 5(c)). Since only 1 DOF is fixed for a misorientation GB, its response is almost identical to that of a random aggregate. In fact, the angular dependence of $\langle\sigma_{nn}/\Sigma\rangle$ and $s(\sigma_{nn}/\Sigma)$ is very weak for all considered cases, irrespective of the number of fixed DOF per GB. It can be observed that GB normal direction, encoded in <*abc*>-twin and <*abc*>-twist GBs, has the largest influence on INS fluctuations (where in the latter case the effect is slightly bigger, see Fig. 5(c)).

An explanation for this observation seems straightforward. It can be expected that the amplitude of GB normal stress reduces if both grains surrounding the GB are softer (in the direction of GB normal) than the surrounding neighborhood (also in the same direction of GB normal). In this way, the applied stress projected along the GB normal would redistribute more over the stiffer bulk than over the softer grains. For γ-Fe grains, this is indeed the case: <001> and <111> directions are respectively the softest and the stiffest crystal directions. As a result, <001>-twist GBs should exhibit the lowest INS fluctuations, while <111>-twist GBs should exhibit the largest INS fluctuations. Both are confirmed in Fig. 5. Note also that Σ3-twist and Σ7-twist GBs belong to a subgroup of <111>-twist GBs (with a twist angle fixed to 60.0^o and 38.2^o, respectively), while Σ5-twist GB to a subgroup of <001>-twist GBs (with a twist angle fixed to 36.9^o) confirming results in Fig. 4. In this respect, the behavior of Σn-twist GBs is therefore dependent mostly on the twist axis (or GB plane) and not on the twist angle.

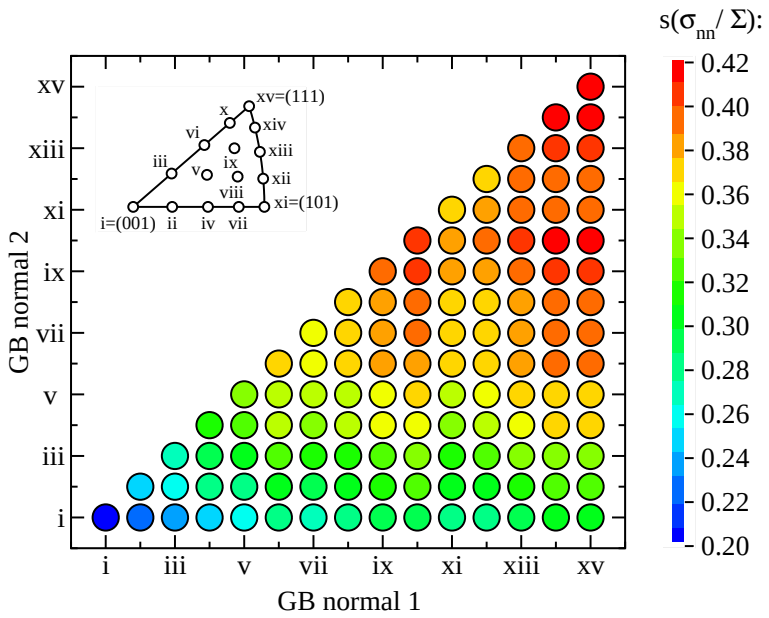

Figure 6. Standard deviation of normalized INS $s(\sigma_{nn}/\Sigma)$ in the Voronoi aggregate model under tensile stress Σ, calculated on embedded (abc)-(def) GBs (17% GB area fraction). Each colored dot (i, j) denotes a response of an aggregate with special GB planes expressed as $i = (abc)$ in one grain and as $j = (def)$ in other grain. 120 such (i, j) dots are shown as a result of selecting i and j among 15 predefined GB planes from the standard stereographic triangle shown in the inset (with their directions *i–xv* listed in the same order in the bottom-most row of Tab. 2). Due to symmetry $(i, j) \rightarrow (j, i)$, only half of the plane is shown. Note that dots on the diagonal with (abc)-(abc) GBs correspond to <abc>-twist GBs (ignoring the effect of a twist angle). Material properties of γ-Fe were used.

Since GB plane has seemingly the largest impact on INS fluctuations, special (abc)-(def) types of GBs are introduced and analysed in Fig. 6. According to the definition given in Tab. 2, four fixed DOF are associated with each (abc)-(def) GB with an additional twist angle between the two grains (fifth DOF) assumed random. As shown in Fig. 5(c), fixing the angle would not contribute significantly to the overall response, leading to

$$s(\sigma_{nn}/\Sigma) = \mathcal{F}(a, b, c, d, e, f, \phi) \approx \mathcal{F}(a, b, c, d, e, f). \tag{2}$$

Here, $\mathcal{F}$ denotes only a functional dependence of $s(\sigma_{nn}/\Sigma)$ and does not refer to any particular mathematical function.

It can be observed in Fig. 6 that aggregates with increased share of (abc)-(def) GBs show very different responses, with INS fluctuations ranging from $s(\sigma_{nn}/\Sigma) \approx 0.20$ to $s(\sigma_{nn}/\Sigma) \approx 0.42$. Both values were already encountered before for <001>-twist GBs (*e.g.*, Σ5-twist) and <111>-twist GBs (*e.g.*, Σ3-twist or Σ7-twist), respectively. The reason is that <abc>-twist GB actually corresponds to (abc)-(abc) GB if the effect of the twist angle is ignored (colored dots on the diagonal of Fig. 6).

The results of Fig. 6 confirm that the smallest INS fluctuations are expected on (001)-(001) GBs and the largest INS fluctuations on (111)-(111) GBs. This is in agreement with the explanation given above since (001)-(001) GBs and (111)-(111) GBs in γ-Fe denote GBs with GB normals oriented along the softest and the stiffest crystal directions of both grains, respectively.

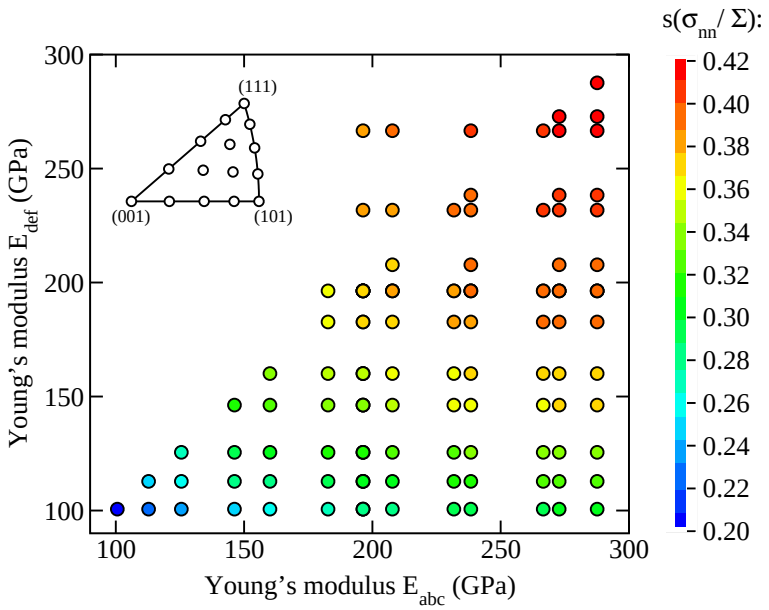

Figure 7. Similar to Fig. 6 but replacing each (i, j) pair by a corresponding pair of Young's moduli (E_{abc}, E_{def}) calculated along the $i = [abc]$ direction in one grain and $j = [def]$ direction in the other grain. The analytical expression for E_{abc} is detailed in Eq. (3). The columns are reshuffled with respect to (arbitrary) indexed directions in stereographic triangle used in Fig. 6 resulting in points above the diagonal. Note also that some of the 120 points overlap due to degeneracy of E_{abc} (here $E_{101} = E_{112} = E_{314}$) whose origin is the degeneracy in the orientation-dependent part of E_{abc} specified in Eq. (4).

Since the above claim is valid for the two extreme directions, it is tempting to rewrite the results obtained on (abc)-(def) GBs in terms of Young's moduli of the two neighboring grains E_{abc} and E_{def}, see Fig. 7. Here, Young's modulus E_{abc} is a measure of grain stiffness for a uniaxial stress applied along the GB normal direction $[abc]$ and can be expressed as (Zhang et al., 2007)

$$\frac{1}{E_{abc}} = \frac{C_{11} + C_{12}}{C_{11}^2 + C_{11}C_{12} - 2C_{12}^2} + \left(\frac{1}{C_{44}} - \frac{2}{C_{11} - C_{12}}\right) \Phi(a, b, c), \tag{3}$$

where

$$\Phi(a, b, c) = \frac{(ab)^2 + (ac)^2 + (bc)^2}{(a^2 + b^2 + c^2)^2}, \tag{4}$$

can assume values between 0 and 1/3. Interestingly, the results of Fig. 7 indeed indicate that $s(\sigma_{nn}/\Sigma)$ calculated on (abc)-(def) GBs depends (mostly) on the corresponding Young's moduli E_{abc} and E_{def}, which measure the stiffness of GB immediate neighborhood. For a given material, therefore INS fluctuations can be further approximated by

$$s(\sigma_{nn}/\Sigma) \approx \mathcal{F}(a, b, c, d, e, f) \approx \mathcal{F}(E_{abc}, E_{def}), \tag{5}$$

using two instead of four independent parameters (since normals $[abc]$ are of unit length). Moreover, due to symmetry $\mathcal{F}(E_{abc}, E_{def}) = \mathcal{F}(E_{def}, E_{abc})$, it is furthermore tempting to check if $s(\sigma_{nn}/\Sigma)$ can be viewed as a function of one single parameter that would denote an effective or average stiffness of GB neighborhood. In this respect, the following simplified bicrystal model is considered.

3.3.1. Bicrystal model approximation

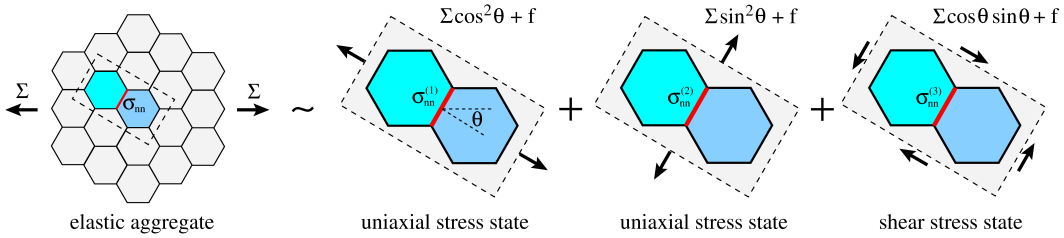

Figure 8. A 2D bicrystal model embedded in elastic aggregate under macroscopic tensile stress Σ. To estimate the local stress acting on the bicrystal neighborhood, the macroscopic stress tensor is first dressed up with fluctuations (f) to account for the anisotropy of far-field grains, then rotated onto a GB plane by angle θ and finally rewritten as a superposition of three simpler cases: two with a uniaxial and one with a shear stress state (with 2D stress amplitudes denoted above). In 3D the same stress decomposition would provide three uniaxial and three shear stress states, with the amplitude of the uniaxial stress mode acting along the GB normal being the same as in 2D, namely $\Sigma\cos(\theta)^2 + f$. Following the principle of linearity, the solution for INS is obtained as a sum of the three partial solutions, $\sigma_{nn} = \sigma_{nn}^{(1)} + \sigma_{nn}^{(2)} + \sigma_{nn}^{(3)}$.

It is assumed that the immediate neighborhood of the (abc)-(def) GB can be described within a bicrystal model embedded in an elastic media, which resembles a far-field neighborhood of a polycrystal. A simplified version of the model in 2D is depicted in Fig. 8 with the proposed strategy for INS estimation using the principles of linearity and superposition. It is easy to realize that for small θ the biggest contribution to INS is coming from the uniaxial stress mode acting along the GB normal, $\sigma_{nn} \sim \sigma_{nn}^{(1)}$. While the contribution of the second uniaxial stress mode is negligible (for small θ), $\sigma_{nn}^{(2)} \sim 0$, the contribution of the shear mode is generally non-zero, $\sigma_{nn}^{(3)} \neq 0$, whereas its average should vanish, $\langle\sigma_{nn}^{(3)}\rangle \sim 0$. Note that similar conclusion holds also in 3D but with different expressions for the stress amplitudes (except for the uniaxial stress mode acting along the GB normal).

Focusing on the first uniaxial stress mode in Fig. 8 for small θ (and omitting the superscript (1)), the continuity of GB normal stress imposes

$$\sigma_{nn} = E_{abc}\epsilon_{nn,1} = E_{def}\epsilon_{nn,2}, \tag{6}$$

where $\epsilon_{nn,1}$ and $\epsilon_{nn,2}$ are respectively the local strains in grains 1 and 2 along the GB normal direction. In the simplest picture, it can be assumed that both $\epsilon_{nn,1}$ and $\epsilon_{nn,2}$ are uniform within the grains and that they recover an average strain of the bicrystal neighborhood,

$$l_1\epsilon_{nn,1} + l_2\epsilon_{nn,2} = (l_1 + l_2)\epsilon_{nn}, \tag{7}$$

where l_1 and l_2 are the lengths of the grains (assumed to be equal, $l_1 = l_2$), and

$$\epsilon_{nn} = \frac{\Sigma\cos(\theta)^2 + f}{\langle E\rangle} \tag{8}$$

is the average strain applied on the bicrystal neighborhood along the GB normal direction. The introduced $\langle E\rangle$ and f represent respectively the Young's modulus of an aggregate and (unknown) stress fluctuations, which arise due to the anisotropy of the grains surrounding the bicrystal neighborhood. From Eqs. (6), (7) and (8), the GB normal stress finally follows as

$$\sigma_{nn} = \frac{2(E_{abc}E_{def})}{(E_{abc} + E_{def})\langle E\rangle}(\Sigma\cos(\theta)^2 + f). \tag{9}$$

The prefactor $2(E_{abc}E_{def})/(E_{abc}+E_{def})$ in the above equation can be seen as an average stiffness measure of the (abc)-(def) GB neighborhood. With further normalization by E_{max} denoting the maximum value of E_{abc} over all possible directions $[abc]$, the following effective Young's modulus is finally defined[5]

$$E_{12} = \frac{2E_{abc}E_{def}}{(E_{abc} + E_{def})E_{max}}. \tag{10}$$

[5] Although normalization by aggregate Young's modulus $\langle E\rangle$ is equivalent and may even seem more natural, the normalization by E_{max} is chosen to provide an exact upper bound, $0 \leq E_{12} \leq 1$.

It is important to highlight that parameter E_{12} does not only depend on the geometry (a, b, c, d, e, f) but also on material properties (C_{11}, C_{12}, C_{44}).

The derived relation $\sigma_{nn} = \mathcal{F}(\Sigma, E_{12}, \langle E \rangle, \theta, f)$ in Eq. (9) is a useful tool to estimate INS despite the fact that stress fluctuations f of the introduced bicrystal model are in principle unknown at a particular GB. However, when integrating over all GB planes (defined by θ) of one particular GB type (defined by E_{12}), the fluctuations should average out in a large untextured aggregate, $\langle f \rangle = 0$, yielding $\langle \sigma_{nn} \rangle = \Sigma \langle \cos\theta^2 \rangle \langle E_{12} \rangle E_{max} / \langle E \rangle = \Sigma/3$, which is indeed observed numerically for all E_{12}.

The situation is, however, less clear when calculating INS fluctuations on a given GB type. In this case the contribution of f to $s(\sigma_{nn}/\Sigma)$ may be substantial and further research is needed to provide the analytical estimate (which may also require to consider shear stress modes, as depicted in Fig. 8 for a 2D bicrystal model). In spite of the uncertainties, the introduced E_{12} is nevertheless found to be a key parameter contributing to the $s(\sigma_{nn}/\Sigma)$ as demonstrated below.

3.3.2. *Grain boundary stiffness parameter*

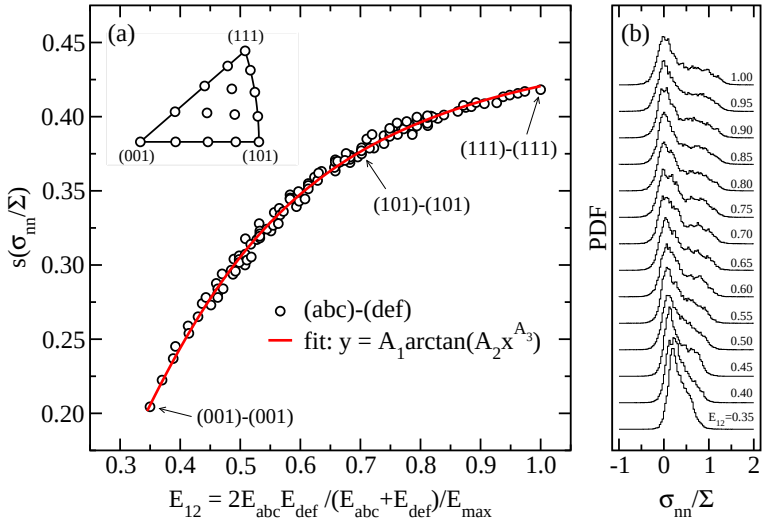

Figure 9. (a) Standard deviation of normalized INS $s(\sigma_{nn}/\Sigma)$ in the Voronoi aggregate model calculated on embedded (abc)-(def) GBs expressed as a function of effective Young's modulus E_{12}, see Eq. (10). Same calculated data are shown as presented in Fig. 7. (b) Probability density functions (PDF) of σ_{nn}/Σ calculated on different (abc)-(def) GBs corresponding to equidistant E_{12} values (plotted on top of each other).

In Fig. 9(a) the results $s(\sigma_{nn}/\Sigma)$ of Fig. 7 are replotted as a function of the newly introduced parameter E_{12}, showing almost a perfect correlation that can be accurately described by an arctan function,

$$s(\sigma_{nn}/\Sigma) \approx \mathcal{F}(E_{12}) = A_1 \arctan\left(A_2 E_{12}^{A_3}\right), \tag{11}$$

using three fitting parameters A_k (see Appendix C for more details). Equations (10) and (11) represent the first main result of this study. Although the selection of the fitting function seems rather arbitrary, it nevertheless shows several strengths especially when used in combination with other materials (see Sec. 4). Also, by design, it naturally implies that $s(\sigma_{nn}/\Sigma) = 0$ when $E_{12} = 0$. This limit corresponds to a GB plane facing a void which has zero stiffness; as stresses are identically zero on such GBs also fluctuations are vanishing there.

Figure 9(b) shows probability density functions of σ_{nn}/Σ calculated for 14 equidistant E_{12} values corresponding to 14 (abc)-(def) GBs. It is clear from the plot that not only $s(\sigma_{nn}/\Sigma)$ but also the distribution of σ_{nn}/Σ is more or less uniquely determined by E_{12} in a given material. Further analysis of the distribution shape evolution with varying E_{12} is left for future studies.

4. Results for general cubic material

To this end, the analysis of elastic γ-Fe polycrystalline aggregates loaded uniaxially has shown that the mean value of INS is independent of GB type on which it is calculated, leading to $\langle\sigma_{nn}/\Sigma\rangle \approx 1/3$.

It has also been demonstrated that the amplitude of INS fluctuations, $s(\sigma_{nn}/\Sigma)$, when evaluated on GBs of one particular type, depends merely on the orientation of GB plane relative to the two adjoining crystal lattices, with a negligible influence of the corresponding twist angle. In this respect, special GBs with undefined GB plane (*e.g.*, misorientation or Σn), have been shown to behave practically as random GBs, see Fig. 5(a).

However, a quite different response has been observed on special GBs with a fixed GB plane (*e.g.*, Σn-twist, Σn-twin or (abc)-(def)). There, $s(\sigma_{nn}/\Sigma)$ has been shown to depend merely on the effective stiffness E_{12} of the two neighboring grains measured along the GB normal direction, leading to $s(\sigma_{nn}/\Sigma) \approx A_1 \arctan(A_2 E_{12}^{A_3})$. For γ-Fe grains in particular, the amplitude has been shown to range between $s(\sigma_{nn}/\Sigma) \approx 0.20$, when calculated on GBs whose normals are oriented along the softest direction <001> in both adjoining grains, and $s(\sigma_{nn}/\Sigma) \approx 0.42$, when calculated on GBs whose normals are oriented along the stiffest direction <111> in both adjoining grains. To generalize the above results, γ-Fe grains are in this section replaced by various other materials.

4.1. Material effect and Zener anisotropy index

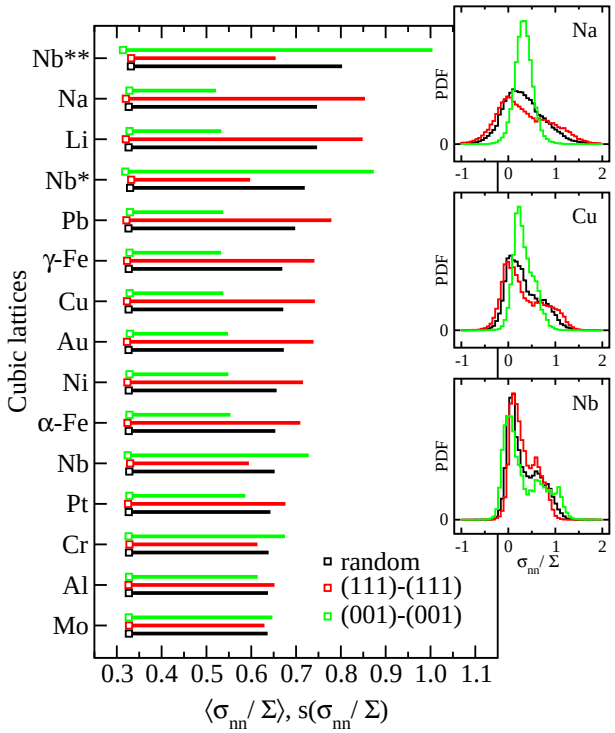

Figure 10. Mean value and standard deviation of normalized INS, $\langle\sigma_{nn}/\Sigma\rangle$ and $s(\sigma_{nn}/\Sigma)$, plotted for various cubic materials from Tab. 1 and with either purely random, (001)-(001) or (111)-(111) GBs (both with 17% GB area fraction) embedded in the Voronoi aggregate model under tensile stress Σ. Insets show distributions of normalized INS calculated for three selected materials.

The influence of various cubic materials from Tab. 1 is analyzed in Fig. 10, showing the responses of random GBs and the two most extreme cases measured on (001)-(001) and (111)-(111) GBs. As different materials are ordered vertically according to their universal elastic anisotropy index A^u (Ranganathan and Ostaja-Starzewski, 2008) (see also Tab. 1), two opposite trends can be observed in Fig. 10. The first group of materials (*e.g.*, Al, Pt, Ni, ...) behaves qualitatively the same as γ-Fe analyzed in the previous section. The corresponding $s(\sigma_{nn}/\Sigma)$ seems to strongly correlate with A^u, which implies that elastic grain anisotropy is the main contributor to the INS fluctuations. While $s(\sigma_{nn}/\Sigma)$ increases monotonically with A^u on (111)-(111) GBs, the trend reverses on (001)-(001) GBs. Note that a

similar monotonically increasing relation between $s(\sigma_{nn}/\Sigma)$ and A^u was rationalized and derived in (El Shawish and Hure, 2018) for random GBs in all polycrystalline materials. This relation can also be recognized here in Fig. 10 for all 15 polycrystals.

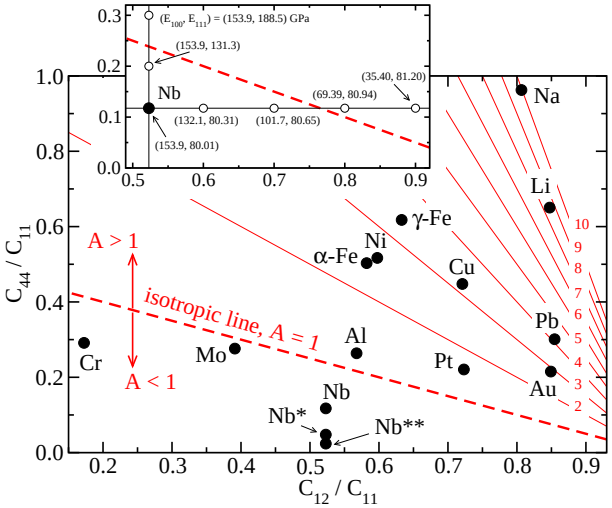

Figure 11. Positions of various cubic materials from Tab. 1 in $C_{12}/C_{11} - C_{44}/C_{11}$ plane. Isotropic line marks the region of isotropic grain behavior with Zener anisotropy index $A = 1$. Inset shows the evolution of Young's moduli of single-crystal Nb-like materials with increasing C_{12}/C_{11} (circles along horizontal line) or increasing C_{44}/C_{11} (circles along vertical line). Young's moduli E_{100} and E_{111} are calculated respectively along [100] and [111] crystal directions using Eq. (3).

The second group of materials in Fig. 10 (*e.g.*, Mo, Cr, Nb) also shows strong dependence on A^u, however, the trend is switched between the (111)-(111) and (001)-(001) GBs. The reason for this is analyzed in detail in Fig. 11, where all investigated materials from Tab. 1 are positioned on the $C_{12}/C_{11} - C_{44}/C_{11}$ plane. In addition, the isotropic line is added to the plane which represents the isotropic crystals with Zener anisotropy index equal to one, $A = 1$. It is clear from this plot that all materials from the second group are placed below the isotropic line where $A < 1$, while all the crystals of the first group lie in the region with $A > 1$.

The inset of Fig. 11 shows the evolution of single-crystal Young's moduli, E_{100} and E_{111}, calculated respectively along [100] and [111] directions, when going from the Nb position in the parameter plane towards (and over) the isotropic line $A = 1$ using two different paths. Stiffness values shown in the inset demonstrate that $E_{100} > E_{111}$ for $A < 1$ and $E_{100} < E_{111}$ for $A > 1$. In other words, the isotropic line represents the border where the stiffest and the softest tensile directions switch in a cubic crystal. Since the two directions for Nb and other materials from the second group are switched (relative to cubic materials of the first group), also the responses on (001)-(001) and (111)-(111) GBs are qualitatively switched as shown in Fig. 10.

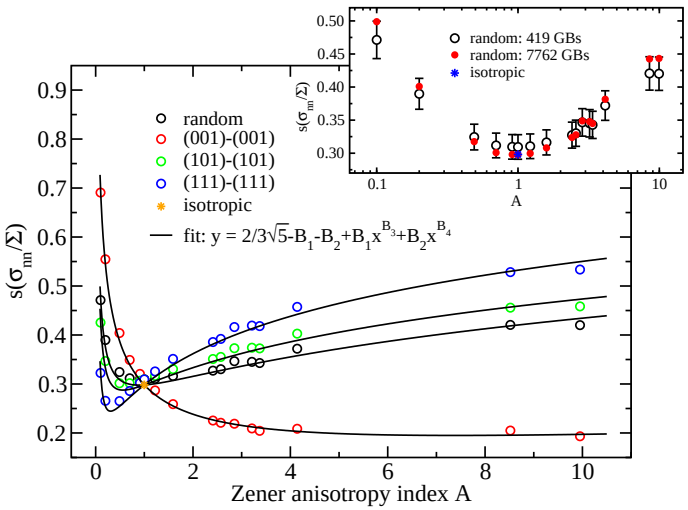

Figure 12. Standard deviation of normalized INS $s(\sigma_{nn}/\Sigma)$ computed on various GB types as a function of Zener anisotropy index A. Results are calculated for all cubic materials from Tab. 1 using either purely random, (001)-(001), (101)-(101) or (111)-(111) GBs (all with 17% GB area fraction) embedded in the Voronoi aggregate model under elastic tensile stress Σ. The modelling function shown can be fitted to all four data sets. The inset compares the results obtained in a purely random Voronoi aggregate model when using either 419 GBs (17% GB area fraction) or 7762 GBs (100% GB area fraction) for the calculation of $s(\sigma_{nn}/\Sigma)$ where the isotropic case (denoted by a blue star) serves as a benchmark point. Error bars denote a relative error of 6%, which can be attributed to the statistically smaller sample.

Following the above discussion, it seems more natural to employ a functional dependence of $s(\sigma_{nn}/\Sigma)$ on Zener anisotropy index A rather than on universal elastic anisotropy index A^u. The proposed correlation between $s(\sigma_{nn}/\Sigma)$ and A is finally shown in Fig. 12 for random GBs and three different special GB types. Indeed, a smooth continuous dependence of $s(\sigma_{nn}/\Sigma)$ on A is utilized for each GB type, showing a switching behavior at the crossing point $A = 1$ as expected. In a similar manner as in Fig. 9, an empirical fitting function can be introduced for each GB type as a function of Zener index A to account for different materials (see Appendix C for more details).

At this point, it is important to highlight that the amplitude of GB normal stress fluctuations, $s(\sigma_{nn}/\Sigma)$, when evaluated on random GBs or special GBs with undefined GB plane (*e.g.*, misorientation or Σn), depends solely on Zener anisotropy index A,

$$s_{\text{random}}(\sigma_{nn}/\Sigma) \approx \mathcal{F}(A). \tag{12}$$

Note that a similar relation between $s(\sigma_{nn}/\Sigma)$ and universal anisotropy index A^u was rationalized and derived in (El Shawish and Hure, 2018).

4.2. Zener anisotropy index and grain boundary stiffness parameter

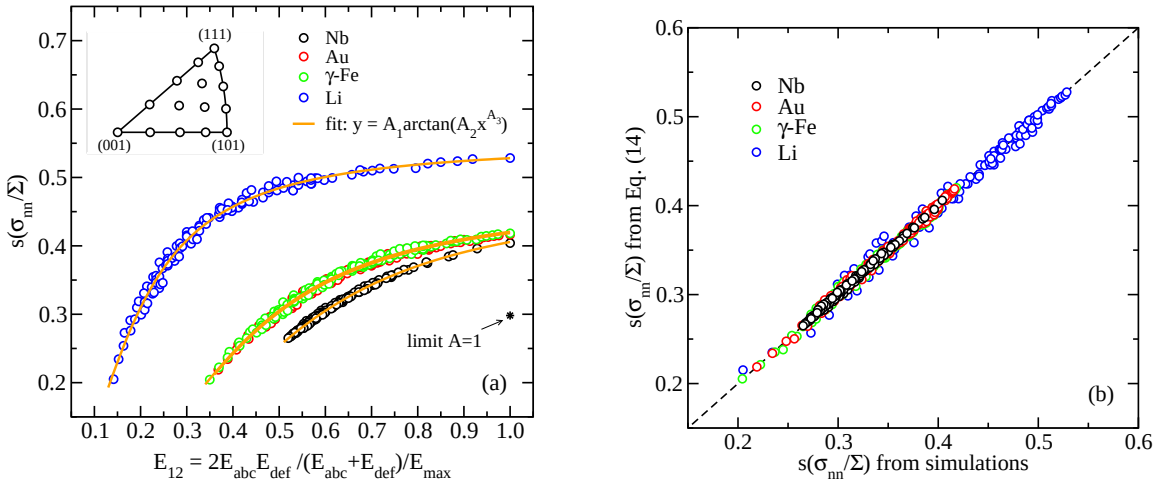

Figure 13. (a) Standard deviation of normalized INS $s(\sigma_{nn}/\Sigma)$ calculated on (abc)-(def) GBs embedded in the Voronoi aggregate model for four selected materials and expressed as a function of effective Young's modulus E_{12}. The modelling function shown can be fitted to all four data sets. In the isotropic limit, $A = 1$, the whole E_{12} domain shrinks to a single point at $E_{12} = 1$ due to orientational invariance of E_{abc}. (b) A comparison of $s(\sigma_{nn}/\Sigma)$ results obtained from finite element simulations and Eq. (14) for four selected materials shown in (a).

The combined effect of using different materials and different (abc)-(def) GB types is finally demonstrated in Fig. 13(a). In the same way as in Fig. 9(a), the results of $s(\sigma_{nn}/\Sigma)$, calculated for four different materials, are plotted as a function of the effective stiffness parameter E_{12}. It is clear from the plot that the accuracy of the assumed relation $s(\sigma_{nn}/\Sigma) \approx \mathcal{F}(E_{12})$ can be confirmed for all considered materials, regardless of the fact that substantial reduction in the number of independent variables from five to one was employed.

To summarize the results obtained on (abc)-(def) GBs, the statistical behavior of GB normal stresses, evaluated as standard deviation $s(\sigma_{nn}/\Sigma)$ in different polycrystalline materials of cubic lattice symmetry, depends merely on two (derived) variables: Zener index A, which characterizes the material elastic anisotropy, and effective stiffness parameter E_{12}, which characterizes the stiffness of GB neighborhood along the GB normal direction,

$$s_{(abc)-(def)}(\sigma_{nn}/\Sigma) \approx \mathcal{F}(A, E_{12}). \tag{13}$$

For the assumed uniaxial macroscopic loading, the relation has been further shown to be well-fitted by

$$s_{(abc)-(def)}(\sigma_{nn}/\Sigma) \approx A_1(A) \arctan\left(A_2(A) E_{12}^{A_3(A)}\right), \tag{14}$$

where E_{12} can be computed analytically for arbitrary GB plane direction (a, b, c, d, e, f) of any chosen material (C_{11}, C_{12}, C_{44}) by Eqs. (3), (4) and (10), and A_k are three material dependent fitting parameters that can be determined numerically for a given A determined by Eq. (1) (see Appendix C for more details). The quality of the proposed fit in Eq. (14) is finally shown in Fig. 13(b).

Finite element results presented in this study have been additionally supported by predictions of a simplified model defined in Appendix D. The model is very similar to the bicrystal model introduced in Sec. 3.3.1, apart from including a full tensorial treatment of the involved quantities. The results of the model show accurate predictions for INS distributions on random GBs as a function of elastic anisotropy and loading conditions, and correct trends for the evolution of standard deviations restricted to special GBs. In this respect, the model can be used as a tool to quickly estimate INS distributions without having to rely on fitting functions.

5. Discussion

5.1. Practical implications

The established relations, Eqs. (12)–(14), enable an accurate estimation of the amplitude of GB normal stress fluc-

tuations on arbitrary GB type embedded in a uniaxially loaded polycrystalline material with cubic lattice symmetry. Three examples of immediate use and one potential application can be given.

5.1.1. *Classification of materials*

To estimate in which material, for a given uniaxial loading Σ, there is a higher probability of finding a GB with normal stress larger than some critical stress, $\sigma_{nn} \geq \sigma_c$, one should compare the $s_{\text{random}}(\sigma_{nn}/\Sigma)$ values, obtained on random GBs, given in Fig. 12 at the corresponding Zener index A of materials in question. Since $\langle\sigma_{nn}/\Sigma\rangle \approx 1/3$ for all materials, a material with bigger $s_{\text{random}}(\sigma_{nn}/\Sigma)$ should provide also a bigger fraction of GBs with $\sigma_{nn} \geq \sigma_c$.[6] In this respect, looking only at the materials shown in Fig. 10, polycrystalline Mo, Al, Cr and Pt should provide the smallest fraction, while polycrystalline Li and Na (deliberately omitting the fictitious Nb**) the biggest fraction of such GBs. It is good to note that universal elastic anisotropy index A^u is an equivalent measure for $s_{\text{random}}(\sigma_{nn}/\Sigma)$. It is important to mention that such kind of analysis can be applied not only to cubic crystals but also to any cubic compound (*e.g.*, NaCl, KCl, LiF, MgO, TiC).

5.1.2. *Classification of grain boundaries*

The second example focuses on a classification of GBs according to their propensity to exhibit large normal stresses. Again, a cubic material under elastic (uniaxial) loading is assumed. For this task to be reasonable, it is important to compare GB types within the same group of GBs (*e.g.*, Σn, Σn-twist, Σn-twin, (abc)-(def)), in order to avoid possible misinterpretations of the results due to overlapping definitions. As already pointed out, GB types that are not defined by GB plane but only by lattice orientations (*e.g.*, misorientation, Σn) yield $s(\sigma_{nn}/\Sigma)$ practically equal to $s_{\text{random}}(\sigma_{nn}/\Sigma)$ of random GBs. For such GB types, therefore, the aforementioned classification is trivial as the relative occurrence of highly stressed GBs is practically identical in all of them.[7] To classify GB types within a given group of GBs that accounts for a GB plane (*e.g.*, (abc)-(def)), it is merely enough to arrange GBs according to their effective stiffness parameter E_{12}, which can be calculated analytically using Eq. (10). Since $s_{(abc)-(def)}(\sigma_{nn}/\Sigma)$ is an increasing function of E_{12}, larger E_{12} means also larger probability for having large normal stresses. In this respect, as already mentioned several times, the smallest and largest fraction of highly stressed GBs can be found among (001)-(001) and (111)-(111) GBs, respectively (or vice versa if $A < 1$).

This kind of E_{12} ordering may be quite easily implemented in any visualization software relevant for material characterization. Of course, beforehand a knowledge of material elastic properties and all relevant GB DOF (lattice orientations and/or GB plane) would be necessary, which can be extracted by, *e.g.*, using Diffraction Contrast Tomography (Ludwig et al., 2008; Johnson et al., 2008) or serial sectioning combined with Electron BackScatter Diffraction (Liang et al., 2020). As a result of such implementation, all GBs belonging to a specific GB type could be visualized in a software by, e.g, using a specified color scheme denoting E_{12} values or even $s(\sigma_{nn}/\Sigma)$ values for the assumed uniaxial loading. In fact, the assumption of uniaxial loading condition would be necessary only when the fitting functions for $s(\sigma_{nn}/\Sigma)$ from this study would be used. In principle, GBs with larger E_{12} would be stiffer and thus larger GB normal stress fluctuations would be expected there, irrespective of the loading type.

5.1.3. *Cracking resistance of CSL grain boundaries*

Different cracking susceptibilities of low-Σ CSL GBs observed experimentally may be related also to different INS fluctuations calculated in Sec. 3.2. Restricting to γ-Fe grains, the observed minimum value of $s(\sigma_{nn}/\Sigma) \approx 0.20$ on Σ5-twist GBs in Fig. 4 is considerably smaller than $s(\sigma_{nn}/\Sigma) \approx 0.30$ for isotropic grains, which means that Σ5-twist GBs exhibit very small INS relatively to other GBs. From the loading point of view, Σ5-twist GB should therefore be very resistant to cracking, however, the actual resistance would be strongly influenced by its strength (associated here with the critical stress σ_c), which may depend on many factors such as GB energy, GB diffusivity, GB precipitation condition, oxidation kinetics, etc. Assuming that GB energy is the main contributor to the GB strength, atomistic calculations for Ni (Olmsted et al., 2009) revealed that GB energy of Σ5-twist GB is ~1.0 J/m^2, which is a bit lower

[6] Whether this implies also a higher probability for intergranular crack initiation (due to IGSCC), depends also or primarily on the strength of a particular GB.

[7] In this respect, the classification of, *e.g.*, Σn GBs according to their propensity for intergranular cracking (due to IGSCC) should be determined entirely by their GB strength.

than the average energy ∼1.2 J/m^2 of a random GB (that otherwise ranges from ∼0.7 to ∼1.5 J/m^2 for Ni), but still roughly two and ten times higher than the energies of Σ7-twist GB (∼0.50 J/m^2) and Σ3-twist GB ($\lesssim$0.1 J/m^2), respectively.[8] In this respect, Σ5-twist GB seems to be weaker than both Σ3-twist and Σ7-twist GBs but stronger, on average, than a random GB. Therefore, in combination with minimal INS fluctuations, Σ5-twist GB should potentially be resistant to cracking (IGSCC).

In a similar way, the maximum value of $s(\sigma_{nn}/\Sigma) \sim 0.42$ obtained for Σ3-twist and Σ7-twist GBs implies that these two GB types exhibit largest INS relatively to other Σn-twist GBs. As already discussed above, a well-known cracking resistance of Σ3-twist GB (coherent Σ3 twin GB in face-centered cubic metals) must originate in very high GB strength, mostly due to very low GB energy (*e.g.*, $\lesssim$0.1 J/m^2 for Ni (Olmsted et al., 2009)). Obviously, the corresponding critical stress is very large so that $\sigma_{nn} < \sigma_c$. However, since GB energy of Σ7-twist GB is about five times higher and INS fluctuations are largest possible, Σ7-twist GB could be potentially (very) prone to cracking.

5.1.4. *Grain boundary engineering*

Finally, another possible application of the results is mentioned in connection to Grain Boundary Engineering. In case a redistribution of different GB types would be possible in a given specimen or component, one could implement a higher fraction of softest GBs (*e.g.*, (001)-(001) for $A > 1$) near a free surface, where IGSCC initiation is more likely to occur, and correspondingly a higher fraction of stiffest GBs (*e.g.*, (111)-(111) for $A > 1$) in the remaining bulk. Of course, for realistic applications, an additional knowledge of GB strengths would be needed to decide for the optimal strategy. Namely, following the well-known cracking resistance of the coherent Σ3 twin GB in face-centered cubic materials, which is actually a subgroup of the (111)-(111) GBs, obviously not all (111)-(111) GBs should be removed from the free surface for this purpose.

In a similar way, one may try to reduce the risk for crack coalescence (formation of a macroscopic crack) in a desired part of a component by adding a sufficient number of special GBs that have a good cracking resistance (either due to smaller $s(\sigma_{nn}/\Sigma)$ and/or larger GB strength).

5.2. *Possible extensions*

The empirical relation in Eq. (14) has been derived assuming uniaxial loading condition and polycrystalline materials with cubic crystal structure. In principle, similar relations can be formulated for other types of loading and/or polycrystals with lower crystal symmetries. However, it is expected that qualitative behavior of GB normal stress fluctuations should remain unchanged: stiffer GBs, characterized by the larger values of the newly introduced effective Young's modulus E_{12}, should produce larger $s(\sigma_{nn}/\Sigma)$.

Another possible direction of future research is to include plastic effects in the evolution of $s(\sigma_{nn}/\Sigma)$ with Σ. Although distributions of INS obtained at the onset of plasticity deviate very gradually from those calculated under purely elastic loads (El Shawish and Hure, 2018), plastic effects become crucial for loads well above the yield stress. In effect, plastic anisotropy of the grains starts to dominate the behavior of the polycrystal so that A (or A^u) becomes insufficient.

An interesting topic to be further addressed is also the evolution of σ_{nn}/Σ distribution with E_{12} and A. So far, only the evolution of the corresponding first two statistical moments, $\langle\sigma_{nn}/\Sigma\rangle$ and $s(\sigma_{nn}/\Sigma)$, has been examined. Since $\langle\sigma_{nn}/\Sigma\rangle$ is practically constant in all materials, the value of $s(\sigma_{nn}/\Sigma)$ has been used, as a first approximation, to measure the occurrence of GBs with large GB normal stresses (*e.g.*, $\sigma_{nn} > \sigma_c$). However, as σ_{nn}/Σ distributions are non-Gaussian (see Fig. 9(b)), higher statistical moments would be required to better estimate the distribution shape and thus the fraction of highly stressed GBs.

Finally, additional theoretical work would be needed to derive an accurate expression for local INS on a given GB type (similar to Eq. (9) but for arbitrary θ), which would allow to predict INS distributions quickly without relying on fitting parameters.

[8] It is important to emphasize that GB energy does not only depend on 5 macroscopic DOF of a GB but very much also on the alloying elements present in the vicinity of a GB. Therefore, the above relative comparison of GB energies for pure Ni does not apply to all materials.

6. Conclusions

In this study, finite element analysis of intergranular normal stresses has been performed in order to identify a possible statistical correlation between the intergranular normal stresses and the corresponding grain boundary type embedded within a polycrystalline aggregate. The analysis has been limited to elastic continuum grains of cubic lattice symmetry and uniaxial macroscopic loading. To obtain meaningful results, first two statistical moments - the mean value and standard deviation - have been analyzed from the calculated intergranular normal stresses obtained on various grain boundary types. The following conclusions have been reached:

- The mean value of intergranular normal stress, $\langle\sigma_{nn}/\Sigma\rangle$, normalized by applied uniaxial stress Σ, has been shown analytically within a simplified bicrystal model and confirmed numerically to be independent of the material and grain boundary type on which it is calculated, leading to $\langle\sigma_{nn}/\Sigma\rangle \approx 1/3$.

- The amplitude of intergranular normal stress fluctuations, $s(\sigma_{nn}/\Sigma)$, when evaluated on one particular grain boundary type, has been shown and explained in simple terms to depend merely on the orientation of the grain boundary plane relative to the two adjoining crystal lattices. In this respect, two groups of grain boundaries have been distinguished: those that have a fixed grain boundary plane, which can thus be expressed as (abc)-(def) grain boundaries (*e.g.*, Σn-twist, Σn-twin), and those that do not (*e.g.*, misorientation, Σn). The response of the latter ones has been shown to be practically identical to the response of random grain boundaries, which - to a good approximation - depends solely on Zener anisotropy index A, $s_{\text{random}}(\sigma_{nn}/\Sigma) \approx \mathcal{F}(A)$.

- The value of $s_{(abc)-(def)}(\sigma_{nn}/\Sigma)$, when evaluated on the (abc)-(def) grain boundaries, has been shown and explained in simple terms to depend merely on two variables: Zener anisotropy index A and a newly introduced effective stiffness parameter E_{12}, which measures the average stiffness of grain boundary neighborhood along the grain boundary normal direction. As the main result, the analytical expression, $E_{12} = \mathcal{F}(C_{ij}, a, b, c, d, e, f)$, and the empirical relation, $s_{(abc)-(def)}(\sigma_{nn}/\Sigma) \approx \mathcal{F}(A, E_{12})$, have been derived.

- Following the above result, the classification of (abc)-(def) grain boundaries according to their propensity to exhibit large normal stresses has been trivially reduced to the calculation of the corresponding effective stiffness parameter E_{12}: larger E_{12} means larger $s_{(abc)-(def)}(\sigma_{nn}/\Sigma)$, which implies larger probability for the occurrence of highly stressed grain boundaries. A possible implementation of the result to a grain boundary visualization software relevant for material characterization has been proposed.

- Two qualitatively different behaviors have been identified on cubic lattices. For crystals with Zener anisotropy index $A > 1$, the minimum amplitude of intergranular normal stress fluctuations s_{min} is obtained on grain boundaries whose normals are oriented along the softest direction <001> in both adjoining grains (*e.g.*, Σ5-twist, <001>-twist, (001)-(001)) corresponding to the minimal E_{12}, and the maximum amplitude s_{max} on grain boundaries whose normals are oriented along the stiffest direction <111> in both adjoining grains (*e.g.*, Σ3-twist, Σ7-twist, <111>-twist, (111)-(111)) corresponding to the maximal E_{12}. For crystals with Zener anisotropy index $A < 1$, the trend is reversed.

- Few practical implications have been discussed relevant to IGSCC of Coincidence Site Lattice grain boundaries. Although the cracking susceptibility of coherent Σ3 twin grain boundary in face-centered cubic metals is very low, it has been highlighted that this grain boundary nevertheless exhibits the largest intergranular normal stresses, $s(\sigma_{nn}/\Sigma) \approx s_{max}$.

Acknowledgments

The authors gratefully acknowledge financial support provided by Slovenian Research Agency (grant P2-0026) and French Atomic Energy Commission.

Appendix A. Visualization of special grain boundaries

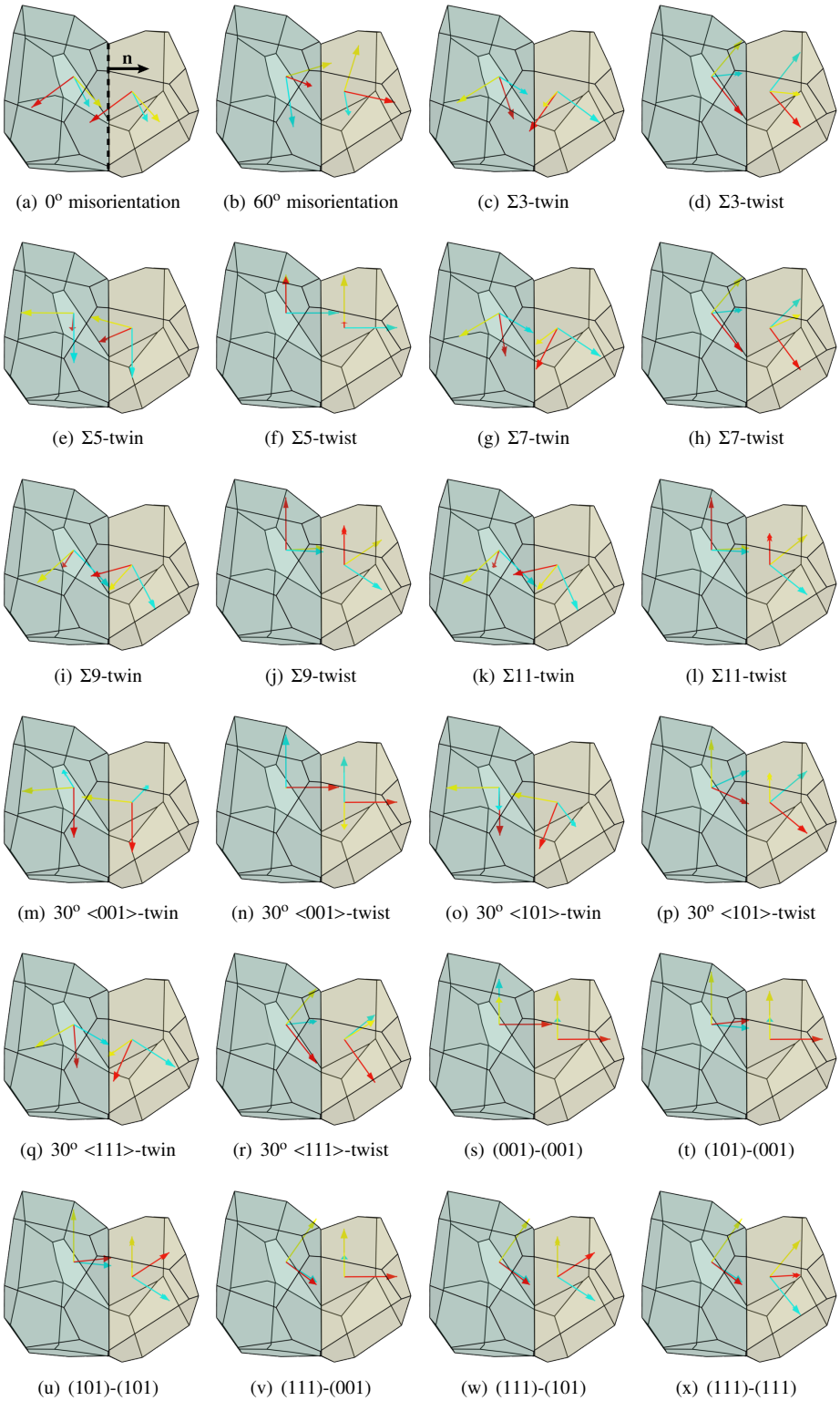

(a) 0° misorientation (b) 60° misorientation (c) Σ3-twin (d) Σ3-twist

(e) Σ5-twin (f) Σ5-twist (g) Σ7-twin (h) Σ7-twist

(i) Σ9-twin (j) Σ9-twist (k) Σ11-twin (l) Σ11-twist

(m) 30° <001>-twin (n) 30° <001>-twist (o) 30° <101>-twin (p) 30° <101>-twist

(q) 30° <111>-twin (r) 30° <111>-twist (s) (001)-(001) (t) (101)-(001)

(u) (101)-(101) (v) (111)-(001) (w) (111)-(101) (x) (111)-(111)

Figure A.14. Orientations of the two grains denoting a special GB. Local axes: [100] (blue), [010] (yellow), [001] (red). GB plane and GB normal ***n*** are indicated in (a).

Appendix B. Convergence analysis

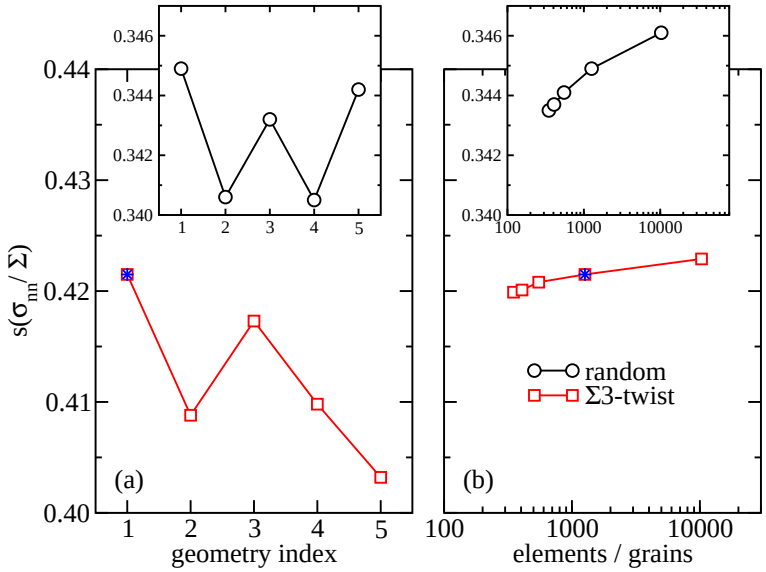

Figure B.15. Standard deviation of normalized INS $s(\sigma_{nn}/\Sigma)$ calculated in a 1000-grain Voronoi aggregate on embedded Σ3-twist GBs (17% GB area fraction) as a function of (a) grain topology and (b) finite element mesh density. The aggregate used in the main study is marked with star symbol. Insets show similar comparisons for the same aggregates but with purely random GBs. Material properties of γ-Fe were used.

In Fig. B.15 finite size effects are estimated on $s(\sigma_{nn}/\Sigma)$ when calculated within a 1000-grain aggregate. In particular, the effects of grain topology (by using different variations of the aggregate shown in Fig. 1(a)) and finite element mesh density are shown. It is observed that dominant finite size effects can be attributed to the (insufficient) aggregate size, manifesting as $\Delta s/\langle s\rangle \approx 0.01/0.41 \lesssim 0.03$ for Σ3-twist GBs and $\Delta s/\langle s\rangle \approx 0.003/0.343 \lesssim 0.01$ for random GBs. The values differ because different number of GBs are considered in the calculation: 419 of Σ3-twist GBs and 7762 of random GBs. Note that the effect of special GBs on $s(\sigma_{nn}/\Sigma)$ is much bigger, providing values between ~0.20 and ~0.42 (see Sec. 3).

Appendix C. Estimation of fitting parameters for uniaxial loading

In Figs. 9 and 13 the numerical results for $s(\sigma_{nn}/\Sigma)$ have been shown to be accurately described by an arctan function of Eq. (14). The corresponding fitting parameters A_k are listed in Tab. C.3.

Material	A_1	A_2	A_3
Nb	0.302	4.34	1.96
Au	0.297	6.17	1.92
γ-Fe	0.297	6.35	1.94
Li	0.350	15.8	1.59

Table C.3. Fitting parameters A_k of the assumed fit $y = A_1 \arctan(A_2 x^{A_3})$ applied to the data presented in Figs. 9 and 13.

The accuracy of the assumed relation $s(\sigma_{nn}/\Sigma) \approx \mathcal{F}(E_{12})$, due to substantial reduction in the number of independent variables from five to one, can be estimated from Fig. 13 for a given material. By visual inspection of the most scattered Li data, an estimated error of $\Delta s \lesssim 0.02$ can be attributed conservatively to the proposed arctan fitting function.

In a similar manner, the numerical results for $s(\sigma_{nn}/\Sigma)$ in Fig. 12 can be accurately described by the following empirical fitting function applicable to each GB type (labeled l),

$$s(\sigma_{nn}/\Sigma) \approx \mathcal{F}(A,l) = 2/(3\sqrt{5}) - B_{1,l} - B_{2,l} + B_{1,l}A^{B_{3,l}} + B_{2,l}A^{B_{4,l}}, \tag{C.1}$$

using four fitting parameters $B_{k,l}$ listed in Tab. C.4. Note that $B_{k,l}$ were obtained on the $0.1 \leq A \leq 10$ range.

GB type l	$B_{1,l}$	$B_{2,l}$	$B_{3,l}$	$B_{4,l}$
random	$9.68\ 10^{2}$	$5.75\ 10^{-1}$	$1.94\ 10^{-4}$	$-3.15\ 10^{-1}$
(001)-(001)	$1.64\ 10^{3}$	$1.08\ 10^{1}$	$4.13\ 10^{-4}$	$-7.21\ 10^{-2}$
(101)-(101)	$8.76\ 10^{2}$	$1.87\ 10^{-1}$	$1.52\ 10^{-4}$	$-5.23\ 10^{-1}$
(111)-(111)	$9.77\ 10^{2}$	$8.20\ 10^{-2}$	$1.42\ 10^{-4}$	$-7.19\ 10^{-1}$

Table C.4. Fitting parameters $B_{k,l}$ of the assumed fit $y = 2/(3\sqrt{5}) - B_{1,l} - B_{2,l} + B_{1,l}x^{B_{3,l}} + B_{2,l}x^{B_{4,l}}$ applied to the data associated with GB type l presented in Fig. 12.

To estimate the accuracy of the proposed fitting function, two aspects can be addressed. The first aspect deals with the modelling error due to finite size effects in an aggregate with 1000 grains. In the isotropic limit, $A = 1$, the value of $s(\sigma_{nn}/\Sigma) = 0.309$ is obtained in the finite element simulation, which is 0.011 (or 3.7%) bigger than the theoretical value $2/(3\sqrt{5}) \approx 0.298$. The difference comes from the fact that $s(\sigma_{nn}/\Sigma)$ is evaluated on 419 special GBs (out of 7762 GBs), which is statistically insufficient to obtain special GB normals distributed uniformly on a sphere (see Fig. 1(d)). In the inset of Fig. 12 a similar comparison is performed in a purely random Voronoi aggregate model when using either 419 GBs or 7762 GBs for the calculation of $s(\sigma_{nn}/\Sigma)$. In the latter case, already a very accurate value of $s(\sigma_{nn}/\Sigma) = 0.298$ is obtained for $A = 1$. On a given range of A, however, the results obtained on either 419 GBs or 7762 GBs are shown to deviate by a maximum of 6%. This finite size error, $\Delta s/s \sim 0.06$, can be conservatively attributed also to the proposed fitting function in Eq. (C.1). Note that numerical error due to applied finite element mesh is estimated to be much smaller, see Appendix B.

The second aspect regarding the accuracy of the proposed fitting function is of physical nature. Although the functional dependence of $s(\sigma_{nn}/\Sigma)$ on A seems smooth and continuous for all practical considerations, it is nevertheless only approximate. As cubic material is characterized by three independent elastic parameters, C_{11}, C_{12} and C_{44}, (or effectively by two, C_{12}/C_{11} and C_{44}/C_{11}, when using normalized quantities), it cannot be uniquely described by only one (derived) parameter such as A. The estimated error due to $s(\sigma_{nn}/\Sigma) \approx \mathcal{F}(A)$ assumption is obtained visually from Fig. 12, by observing the scatter of data points along the imagined smooth line, of the order of the point size, which amounts to $\Delta s \sim 0.02$. Both, the intrinsic error, $\Delta s \sim 0.02$, and numerical finite size error, $\Delta s/s \sim 0.06$, dictate the accuracy of the proposed fitting function.

Empirical expression in Eq. (14) for $s_{(abc)-(def)}(\sigma_{nn}/\Sigma)$ calculated on (abc)-(def) GBs for the assumed uniaxial macroscopic loading contains three material-dependent fitting parameters $A_k(A)$ whose values for four selected materials are listed in Tab. C.3. They can be determined numerically, for any given A, from the following three relations (using short GB type notation GB1 ≡ (001)-(001), GB2 ≡ (101)-(101) and GB3 ≡ (111)-(111))

$$\begin{aligned}
A_1 \arctan\left(A_2 E_{12,\mathrm{GB1}}^{A_3}\right) &= 2/(3\sqrt{5}) - B_{1,\mathrm{GB1}} - B_{2,\mathrm{GB1}} + B_{1,\mathrm{GB1}}A^{B_{3,\mathrm{GB1}}} + B_{2,\mathrm{GB1}}A^{B_{4,\mathrm{GB1}}} \\
A_1 \arctan\left(A_2 E_{12,\mathrm{GB2}}^{A_3}\right) &= 2/(3\sqrt{5}) - B_{1,\mathrm{GB2}} - B_{2,\mathrm{GB2}} + B_{1,\mathrm{GB2}}A^{B_{3,\mathrm{GB2}}} + B_{2,\mathrm{GB2}}A^{B_{4,\mathrm{GB2}}} \\
A_1 \arctan\left(A_2 E_{12,\mathrm{GB3}}^{A_3}\right) &= 2/(3\sqrt{5}) - B_{1,\mathrm{GB3}} - B_{2,\mathrm{GB3}} + B_{1,\mathrm{GB3}}A^{B_{3,\mathrm{GB3}}} + B_{2,\mathrm{GB3}}A^{B_{4,\mathrm{GB3}}}
\end{aligned} \tag{C.2}$$

with $B_{k,l}$ listed in Tab. C.4, and

$$\begin{aligned}
E_{12,\mathrm{GB1}} &= \frac{(C_{11}-C_{12})(C_{11}+2C_{12}+C_{44})}{3(C_{11}+C_{12})C_{44}} \\
E_{12,\mathrm{GB2}} &= \frac{4(C_{11}-C_{12})(C_{11}+2C_{12}+C_{44})}{3(C_{11}^2-2C_{12}^2+C_{11}(C_{12}+2C_{44}))} \\
E_{12,\mathrm{GB3}} &= 1
\end{aligned} \tag{C.3}$$

if $A > 1$ or

$$\begin{aligned} E_{12,\mathrm{GB1}} &= 1 \\ E_{12,\mathrm{GB2}} &= \frac{4(C_{11}+C_{12})C_{44}}{C_{11}^2 - 2C_{12}^2 + C_{11}(C_{12}+2C_{44})} \\ E_{12,\mathrm{GB3}} &= \frac{3(C_{11}+C_{12})C_{44}}{(C_{11}-C_{12})(C_{11}+2C_{12}+C_{44})} \end{aligned} \tag{C.4}$$

if $A < 1$, respectively. The need to distinguish between the two cases follows from the fact that qualitative behavior of $s(\sigma_{nn}/\Sigma)$ is switched at the isotropic point, yielding $E_{max} = E_{111}$ for $A > 1$ and $E_{max} = E_{001}$ for $A < 1$ in Eq. (10). Consequently the values of E_{12} for a chosen material can only range between $E_{12,\mathrm{GB1}}$ and 1 (if $A > 1$) or between $E_{12,\mathrm{GB3}} = 1/E_{12,\mathrm{GB1}}$ and 1 (if $A < 1$).

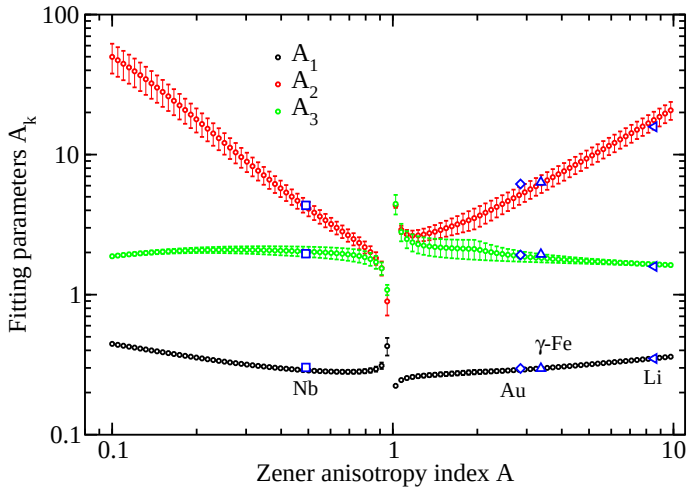

Figure C.16. Fitting parameters A_k as a function of Zener anisotropy index A. A_k are obtained by numerically solving Eqs. (C.2) for $0 < C_{12}/C_{11} < 1$ and $0 < C_{44}/C_{11} < 1$. For a given A, a range of solutions is obtained which is marked by a symbol (denoting an average) and error bars (denoting a range). For comparison, also A_k for four materials from Tab. C.3 are included.

For convenience, the fitting parameters $A_k(A)$, obtained numerically by solving Eqs. (C.2) and using $B_{k,l}$ from Tab. C.4, are shown in Fig. C.16 for the assumed range of elastic properties, $0 < C_{12}/C_{11} < 1$, $0 < C_{44}/C_{11} < 1$ and $0.1 \leq A \leq 10$. Since $s(\sigma_{nn}/\Sigma)$ is not uniquely determined by A for a given GB type, due to existence of materials with same Zener index but different elastic constants resulting in different values of E_{12} for the same GB type, a range of solutions for A_k is obtained at fixed A. However, this range should not be mistaken for an error of A_k; as soon as the elastic constants C_{ij} are known, a unique set of A_k should follow easily from Eqs. (C.2).

Appendix D. Simplified model

Finite element simulations have shown that, in the elastic regime, INS arise mostly from short-range interactions (Fig. 3). This observation opens the way to simplified models for estimating distributions of INS. Let us consider two neighboring grains in a polycrystalline aggregate with grain boundary normal $\boldsymbol{n}$ (Fig. D.17). The fourth-order elasticity tensors of each grain in the GB frame $\{\boldsymbol{n}, \boldsymbol{t}_1, \boldsymbol{t}_2\}$ are noted $\underline{\boldsymbol{K}}_1$ and $\underline{\boldsymbol{K}}_2$, respectively. The average strain of this bicrystal is equal to $\boldsymbol{E}_b$. The mechanical equilibrium imposes that strain tensors $\boldsymbol{E}_1$ and $\boldsymbol{E}_2$ are constant in each grain, and the components are set by the following equations ensuring stress continuity and strain compatibility across the grain boundary, as well as to recover the average strain of the bicrystal:

$$\begin{aligned} &\text{Stress continuity} && (\underline{\boldsymbol{K}}_1 : \boldsymbol{E}_1).\boldsymbol{n} = (\underline{\boldsymbol{K}}_2 : \boldsymbol{E}_2).\boldsymbol{n} \\ &\text{Strain compatibility} && \boldsymbol{t}_i.\boldsymbol{E}_1.\boldsymbol{t}_j = \boldsymbol{t}_i.\boldsymbol{E}_2.\boldsymbol{t}_j \\ &\text{Average strain} && V_1\boldsymbol{E}_1 + V_2\boldsymbol{E}_2 = (V_1+V_2)\boldsymbol{E}_b \end{aligned} \tag{D.1}$$

where V_1 and V_2 are the volumes of each grain. The system of equations (Eqs. D.1) allows to compute all components of the strain tensors, and to finally compute the INS as:

$$\sigma_{nn} = \boldsymbol{n}.(\underline{\boldsymbol{K}}_1 : \boldsymbol{E}_1).\boldsymbol{n} = \boldsymbol{n}.(\underline{\boldsymbol{K}}_2 : \boldsymbol{E}_2).\boldsymbol{n} \tag{D.2}$$

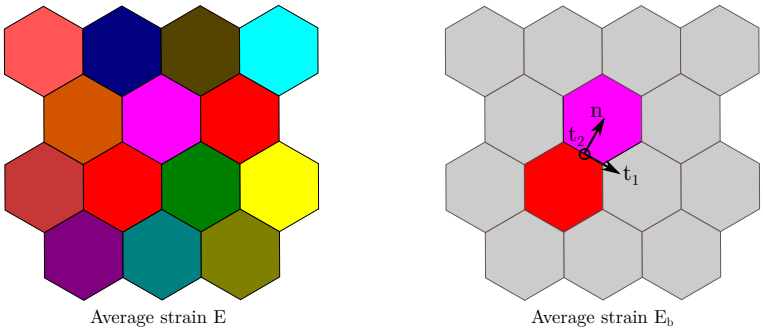

Figure D.17. Polycrystalline aggregate subjected to an average stress $\boldsymbol{\Sigma}$ and strain $\boldsymbol{E}$. Two adjacent grains sharing a boundary of normal $\boldsymbol{n}$ are subjected to an average strain $\boldsymbol{E}_b$.

An assumption should be made for the bicrystal average strain tensor $\boldsymbol{E}_b$ which is set equal to the macroscopic strain of the polycrystalline aggregate $\boldsymbol{E}$. This assumption can be seen as a Voigt-like assumption (Voigt, 1928) but at the bicrystal scale. As distributions of INS are searched for given applied stress conditions, the last ingredient is the relation between stresses and strains at the aggregate scale. Restricting to untextured elastic polycrystalline aggregate, isotropic Hooke's law holds at the aggregate scale:

$$\boldsymbol{E} = \frac{1+\nu}{Y}\boldsymbol{\Sigma} - \frac{\nu}{Y}\,(\mathrm{trace}\,\boldsymbol{\sigma})\,\boldsymbol{I} \tag{D.3}$$

where Y and ν are the Young's modulus and Poisson ratio, respectively. The compression K and shear G elastic moduli can be estimated by the self-consistent approach (Kröner, 1958) that is known to lead to accurate results. For cubic materials they are:

$$\begin{cases} 3K = C_{11} + 2C_{12} \\ 8G^3 + (5C_{11} + 4C_{12})G^2 - C_{44}(7C_{11} - 4C_{12})G - C_{44}(C_{11} - C_{12})(C_{11} + 2C_{12}) = 0 \end{cases} \tag{D.4}$$

and can be used to compute the Young's modulus $Y = 9KG/(3K+G)$ and the Poisson's ratio $\nu = (3K-2G)/(2G+6K)$. For a given material and stress conditions, Eqs. (D.1)–(D.4) can be used to estimate the normal stress at the boundary between two grains. Assuming distributions for the orientation of the normal $\boldsymbol{n}$ and the crystallographic orientations of the grains, a Monte-Carlo like simulation can be done to obtain the distribution of INS of a polycrystalline aggregate. The implementation of the model has been done using the `MTEX` toolbox (Bachmann et al., 2010) of the `Matlab` software, in particular to compute the rotation of the elasticity tensors from the crystallographic frame to the GB frame.

This simplified model is compared to the results of the finite element simulations assuming randomly distributed GB normal for three different materials, Al, γ-Fe and Na, and two different stress loading conditions, uniaxial $\boldsymbol{\Sigma} = \Sigma e_x \otimes e_x$ and equibiaxial $\boldsymbol{\Sigma} = \Sigma(e_x \otimes e_x + e_y \otimes e_y)$. Figure D.18 shows that this simplified model is able to capture quantitatively the INS distributions for random GBs as a function of both elastic anisotropy and loading conditions. Such agreement is an important result as it allows to estimate INS distributions quickly without having to perform finite element simulations. The approach is however more costly than the analytical formulae proposed and calibrated in this study.

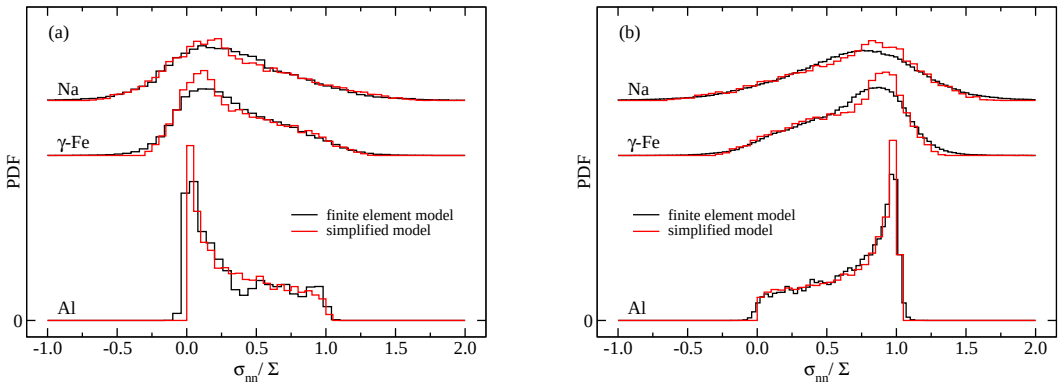

Figure D.18. Comparisons of probability density functions (PDF) of normalized INS of untextured polycrystalline aggregates obtained with finite element simulations and the simplified model for (a) uniaxial and (b) equibiaxial stress loading conditions.

For special GBs, *e.g.*, Σn twist or twin, the model is however not able to capture quantitatively the shape of the INS distributions. Still, the trends for the dependence of standard deviations with respect to anisotropy and special GB type are recovered, as shown in Fig. D.19 where for example the low values of standard deviations for Σ5-twist and twin GBs are captured by the model.

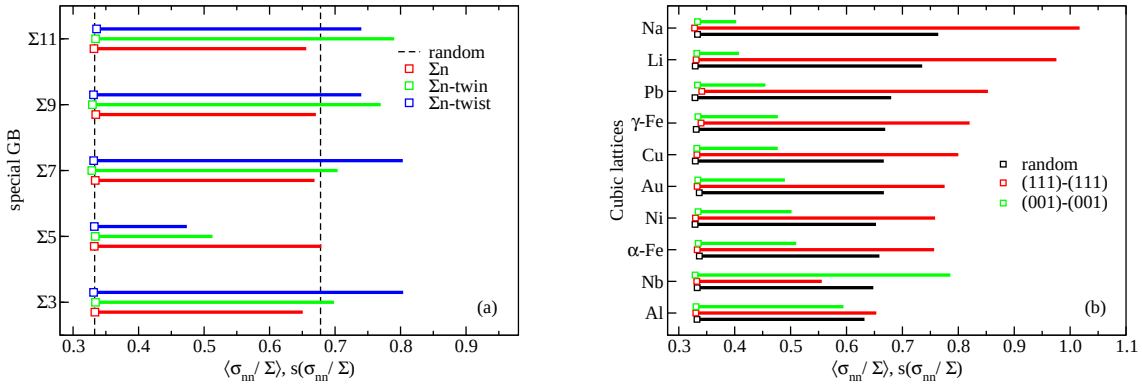

Figure D.19. First and second moments of normalized INS distributions as a function of (a) CSL GB type for γ-Fe and (b) different GB types for various materials. For comparison see Figs. 4 and 10.

The simplified model defined by Eqs. (D.1)–(D.4) leads to accurate predictions on random GBs as a function of elastic anisotropy and loading conditions, and to correct trends for the evolution of standard deviations restricted to special GBs. Therefore, this model can be used as a tool to quickly estimate INS distributions without having to perform finite element simulations and appears as an alternative to the formulae derived and calibrated in this study. Besides, the justification of the validity of the model and its improvement from a theoretical point of view is an interesting question which is left for future research.

References

D. An, T. A. Griffiths, P. Konijnenberg, S. Mandal, Z. Wang, and S. Zaefferer. Correlating the five parameter grain boundary character distribution and the intergranular corrosion behaviour of a stainless steel using 3d orientation microscopy based on mechanical polishing serial sectioning. *Acta. Mat.*, 156:297–309, 2018.

M.A. Arafin and J.A. Szpunar. A new understanding of intergranular stress corrosion cracking resistance of pipeline steel through grain boundary character and crystallographic texture studies. *Corrosion Science*, 51:119–128, 2009.

F. Bachmann, R. Hielscher, and H Schaeben. Texture analysis with MTEX - free and open source software toolbox. *Solid State Phenomena*, 160: 63–68, 2010.

A. F. Bower. *Applied Mechanics of Solids*. Taylor & Francis Group, 2010.

T.D. Burleigh. The postulated mechanisms for stress corrosion cracking of aluminum alloys: A review of the literature 1980-1989. *Corrosion*, 47: 89–98, 1991.

B. Cox. Environmentally induced cracking of zirconium alloys. Technical report, Atomic Energy of Canada Limited, 1970.

B. Cox. Envrionmentally-induced cracking of zirconium alloys - A review. *J. Nuc. Mat*, 170:1–23, 1990.

O. Diard, S. Leclercq, G. Rousselier, and G. Cailletaud. Distribution of normal stress at grain boundaries in multicrystals: Application to an intergranular damamge modeling. *Comp. Mat. Sci.*, 25:73–84, 2002.

O. Diard, S. Leclercq, G. Rousselier, and G. Cailletaud. Evaluation of finite element based analysis of 3D multicrystalline aggregates plasticity. Application to crystal plasticity model identification and the study of strain fields near grain boundaries. *Int. J. Plasticity*, 21:691–722, 2005.

S. El Shawish and J. Hure. Intergranular normal stress distributions in untextured polycrystalline aggregates. *Eur. J. Mech. / A Solids*, 72:354–373, 2018.

S. El Shawish, P. G. Vincent, H. Moulinec, L. Cizelj, and L. Gélébart. Full-field polycrystal plasticity simulations of neutron-irradiated austenitic stainless steel: A comparison between fe and fft-based approaches. *J. Nuc. Mat.*, 529:151927, 2020.

T. Fujii, K. Tohgo, Y. Mori, Y. Miura, and Y. Shimamura. Crystallographic and mechanical investigation of intergranular stress corrosion crack initiation in austenitic stainless steel. *Mat. Sci. Eng. A*, 751:160–170, 2019.

V. Y. Gertsman and S. M. Bruemmer. Study of grain boundary character along intergranular stress corrosion crack paths in austenitic alloys. *Acta Materialia*, 49(9):1589 – 1598, 2001.

D. Gonzalez, I. Simonovski, P.J. Withers, and J. Quinta da Fonseca. Modelling the effect of elastic and plastic anisotropies on stresses at grain boundaries. *Int. J. Plasticity*, 61:49–63, 2014.

J. Gupta, J. Hure, B. Tanguy, L. Laffont, M.C. Lafont, and E. Andrieu. Evaluation of stress corrosion cracking of irradiated 304 stainless steel in PWR environment using heavy ion irradiation. *J. Nuc. Mat.*, 476:82–92, 2016.

J. Hure, S. El Shawish, L. Cizelj, and B. Tanguy. Intergranular stress distributions in polycrystalline aggregates of irradiated stainless steel. *J. Nuc. Mat.*, 2016.

IAEA. Stress corrosion cracking in light water reactors: Good practices and lessons learned. NP-T-3.13, IAEA Nuclear Energy Series, 2011.

D. C. Johnson, B. Kuhr, D. Farkas, and G. S. Was. Quantitative linkage between the stress at dislocation channel grain boundary interaction sites and irradiation assisted stress corrosion crack initiation. *Acta Materialia*, 170:166 – 175, 2019.

G. Johnson, A. King, M. G. Honnicke, J. Marrow, and W. Ludwig. X-ray diffraction contrast tomography: a novel technique for three-dimensional grain mapping of polycrystals. ii. the combined case. *J. Appl. Cryst.*, 41:310–318, 2008.

A.K. Kanjarla, P. Van Houtte, and L. Delannay. Assessment of plastic heterogeneity in grain interaction models using crystal plasticity finite element method. *Int. J. Plasticity*, 26:1220–1233, 2010.

E. Kröner. Berechnung der elastischen konstanten des vielkristalls aus den konstanten des einskristalls. *Z. Physik*, 151:504, 1958.

M. Le Millier, O. Calonne, J. Crépin, C. Duhamel, L. Fournier, F. Gaslain, E. Héripré, O. Toader, Y. Vidalenc, and G. Was. Influence of strain localization on IASCC of proton irradiated 304L stainless steel in simulated PWR primary water. In *16th International Conference on Environmental Degragation of Materials in Nuclear Power Systems - Water Reactors*, 2013.

R.A. Lebensohn, A.K. Kanjarla, and P. Eisenlohr. An elasto-viscoplastic formulation based on fast fourier transforms for the prediction of micromechanical fields in polycrystalline materials. *Int. J. Plasticity*, 32-33:59–69, 2012.

D. Liang, J Hure, A. Courcelle, S. El Shawish, and B. Tanguy. A micromechanical analysis of intergranular stress corrosion cracking of an irradiated austenitic stainless steel. *under review*, 2020.

T. Liu, S. Xia, Q. Bai, B. Zhou, Y. Lu, and T. Shoji. Evaluation of grain boundary network and improvement of intergranular cracking resistance in 316l stainless steel after grain boundary engineering. *Materials*, 12:242–258, 2019.

W. Ludwig, S. Schmidt, E. M. Lauridsen, and H. F. Poulsen. X-ray diffraction contrast tomography: a novel technique for three-dimensional grain mapping of polycrystals. i. direct beam case. *J. Appl. Cryst.*, 41:302–309, 2008.

J. K. Mackenzie. Second paper on statistics associated with the random disorientation of cubes. *Biometrika*, 45:229–240, 1958.

H. Nishioka, K. Fukuya, K. Fujii, and T. Torimaru. IASCC initiation in highly irradiated stainless steels under uniaxial constant load conditions. *J. Nuc. Sci. and Tech.*, 45:1072–1077, 2008.

D. L. Olmsted, S. M. Foiles, and E. A. Holm. Survey of computed grain boundary properties in face-centered cubic materials: I. grain boundary energy. *Acta. Mat.*, 57:3694–3703, 2009.

J. Panter, B. Viguier, J.M. Cloué, M. Foucault, P. Combrade, and E. Andrieu. Influence of oxide films on primary water stress corrosion cracking initiation of alloy 600. *J. Nuc. Mat.*, 348:213–221, 2006.

R. Quey, P. R. Dawson, and F. Barbe. Large-scale 3d random polycrystals for the finite element method: Generation, meshing and remeshing. *Comput. Methods Appl. Mech. Eng.*, 200:1729–1745, 2011.

S. Rahimi and T. J. Marrow. Effects of orientation, stress and exposure time on short intergranular stress corrosion crack behaviour in sensitised type 304 austenitic stainless steel. *Fatigue Fract. Eng. Mater. Struct.*, 35:359–373, 2011.

S. Rahimi, D. L. Engelberg, J. A. Duff, and T. J. Marrow. In situ observation of intergranular crack nucleation in a grain boundary controlled austenitic stainless steel. *Journal of Microscopy*, 233(3):423–431, 2009.

S. I. Ranganathan and M. Ostaja-Starzewski. Universal elastic anisotropy index. *Phys. Rev. Lett.*, 101:055504, 2008.

C.H. Shen and P.G. Shewmon. A mechanism for hydrogen-induced intergranular stress corrosion cracking in alloy 600. *Metall. Trans. A.*, 21A: 1261–1271, 1990.

Simulia. *ABAQUS 6.14-2*, 2016.

M.O. Speidel. Stress corrosion cracking of aluminum alloys. *Metallurgical and Materials Transactions A*, 6A:631–651, 1975.

K.J. Stephenson and G.S. Was. Crack initiation behavior of neutron irradiated model and commercial stainless steels in high temperature water. *J. Nuc. Mat.*, 444:331–341, 2014.

A. Stratulat, J. A. Duff, and T. J. Marrow. Grain boundary structure and intergranular stress corrosion crack initiation in high temperature water of a thermally sensitised austenitic stainless steel, observed in situ. *Corrosion Science*, 85:428 – 435, 2014.

D. Van Rooyen. Review of the stress corrosion cracking of inconel 600. *Corrosion*, 31:327–337, 1975.

W. Voigt. *Lehrbuch der Kristallphysik*. Teubner, 1928.

Z.F. Wang and A. Atrens. Initiation of stress corrosion cracking for pipeline steels in a carbonate-bicarbonate solution. *Metallurgical and Materials Transactions A*, 27A:2686–2691, 1996.

E. A. West and G. S. Was. A model for the normal stress dependence of intergranular cracking of irradiated 316l stainless steel in supercritical water. *Journal of Nuclear Materials*, 408(2):142 – 152, 2011.

Inc. Wolfram Research. Mathematica, Version 10.0. Champaign, IL, 2014.

C. Zener. *Elasticity and Anelasticity of Metals*. University of Chicago, 1948.

J. M. Zhang, Y. Zhang, K. W. Xu, and V. Ji. Young's modulus surface and poisson's ratio curve for cubic metals. *J. Phys. Chem. Solids*, 68: 503–510, 2007.

Z. Zhang, S. Xia, Q. Bai, T. Liu, H. Li, B. Zhou, L. Wang, and W. Ma. Effects of 3-d grain boundary geometrical angles and the net normal stress on intergranular stress corrosion cracking initiation in a 316 stainless steel. *Materials Science and Engineering: A*, 765:138277, 2019.